

## A single cell atlas of human and mouse white adipose tissue

Margo P. Emont<sup>1,2</sup>, Christopher Jacobs<sup>1,2</sup>, Adam L. Essene<sup>1</sup>, Deepti Pant<sup>1</sup>, Danielle Tenen<sup>1,2</sup>, Georgia Colleluori<sup>3</sup>, Angelica Di Vincenzo<sup>3</sup>, Anja M. Jørgensen<sup>4</sup>, Hesam Dashti<sup>2</sup>, Adam Stefek<sup>2</sup>, Elizabeth McGonagle<sup>2</sup>, Sophie Strobel<sup>2</sup>, Samantha Laber<sup>2†</sup>, Saaket Agrawal<sup>2,5</sup>, Gregory P. Westcott<sup>1</sup>, Amrita Kar<sup>1,2</sup>, Molly L. Veregge<sup>1</sup>, Anton Gulko<sup>1</sup>, Harini Srinivasan<sup>1,2</sup>, Zachary Kramer<sup>1</sup>, Eleanna De Filippis<sup>1</sup>, Erin Merkel<sup>1</sup>, Jennifer Ducie<sup>6</sup>, Christopher G. Boyd<sup>7</sup>, William Gourash<sup>8</sup>, Anita Courcoulas<sup>8</sup>, Samuel J. Lin<sup>9</sup>, Bernard T. Lee<sup>9</sup>, Donald Morris<sup>9</sup>, Adam Tobias<sup>9</sup>, Amit V. Khera<sup>2,5,14</sup>, Melina Claussnitzer<sup>2,10</sup>, Tune H. Pers<sup>4</sup>, Antonio Giordano<sup>3</sup>, Orr Ashenberg<sup>11</sup>, Aviv Regev<sup>11,12,13</sup>, Linus T. Tsai<sup>1,2,14</sup>, Evan D. Rosen<sup>1,2,14</sup>

1. Division of Endocrinology, Diabetes and Metabolism, Beth Israel Deaconess Medical Center, Boston, MA, USA
2. Broad Institute of MIT and Harvard, Cambridge, MA, USA
3. Department of Experimental and Clinical Medicine, Center of Obesity, Marche Polytechnic University, Ancona, Italy.
4. Novo Nordisk Foundation Center for Basic Metabolic Research, University of Copenhagen, Copenhagen, Denmark
5. Center for Genomic Medicine, Department of Medicine, Massachusetts General Hospital, Boston, MA, USA
6. Division of Gynecologic Oncology, Department of Obstetrics and Gynecology, Beth Israel Deaconess Medical Center, Boston, MA, USA
7. Department of Surgery, Beth Israel Deaconess Medical Center, Boston, MA, USA

8. Department of Surgery, University of Pittsburgh Medical Center, Pittsburgh, PA
9. Division of Plastic Surgery, Department of Surgery, Beth Israel Deaconess Medical Center, Boston, MA
10. Diabetes Unit and Center for Genomic Medicine, Massachusetts General Hospital, Boston, Massachusetts, 02114, USA.
11. Klarman Cell Observatory, Broad Institute of MIT and Harvard, Cambridge, MA, USA
12. Howard Hughes Medical Institute, Koch Institute of Integrative Cancer Research, Department of Biology, Massachusetts Institute of Technology, Cambridge, MA, USA
13. Genentech, South San Francisco, CA, USA
14. Harvard Medical School, Boston, MA

† Affiliated with Broad Institute while research was conducted

**Address correspondence to:**

Evan D. Rosen, MD PhD

Division of Endocrinology, Diabetes, and Metabolism

Beth Israel Deaconess Medical Center

330 Brookline Avenue

Boston, MA 02215

[erosen@bidmc.harvard.edu](mailto:erosen@bidmc.harvard.edu)

1 **ABSTRACT**

2 **White adipose tissue (WAT), once regarded as morphologically and functionally bland, is**  
3 **now recognized to be dynamic, plastic, heterogenous, and involved in a wide array of**  
4 **biological processes including energy homeostasis, glucose and lipid handling, blood**  
5 **pressure control, and host defense<sup>1</sup>. High fat feeding and other metabolic stressors cause**  
6 **dramatic changes in adipose morphology, physiology, and cellular composition<sup>1</sup>, and**  
7 **alterations in adiposity are associated with insulin resistance, dyslipidemia, and type 2**  
8 **diabetes (T2D)<sup>2</sup>. Here, we provide detailed cellular atlases of human and murine**  
9 **subcutaneous and visceral white fat at single cell resolution across a range of body weight.**  
10 **We identify subpopulations of adipocytes, adipose stem and progenitor cells (ASPCs),**  
11 **vascular, and immune cells and demonstrate commonalities and differences across species**  
12 **and dietary conditions. We link specific cell types to increased risk of metabolic disease,**  
13 **and we provide an initial blueprint for a comprehensive set of interactions between**  
14 **individual cell types in the adipose niche in leanness and obesity. These data comprise an**  
15 **extensive resource for the exploration of genes, traits, and cell types in the function of WAT**  
16 **across species, depots, and nutritional conditions.**

17

18 **A single cell atlas of human white adipose tissue**

19 Mature adipocytes are too large and fragile to withstand traditional single cell approaches; as  
20 a result, several groups have focused on the non-adipocyte stromal-vascular fraction (SVF) of  
21 mouse<sup>3-6</sup> and human<sup>7</sup> adipose tissue. An alternative strategy involves single nucleus (sNuc)  
22 sequencing, which can capture adipocytes, and has been used to describe murine epididymal<sup>8,9</sup>  
23 and human brown adipose tissue<sup>10</sup>. To compare these approaches in the context of human WAT,

24 we pursued experiments on two cohorts of subjects. In the first, we collected subcutaneous WAT  
25 from 9 women, isolated single cells from the SVF using collagenase digestion, and then  
26 performed whole cell Drop-seq [hereafter referred to as single cell (sc)RNA-seq]. Because  
27 different depots have been differentially linked to metabolic disease<sup>11</sup>, for the second cohort we  
28 collected paired subcutaneous (SAT) and omental visceral (VAT) adipose tissue from 10  
29 individuals, and SAT alone from three additional individuals (10 women, 3 men), and performed  
30 sNuc-seq (**Figures 1a, b, and Extended Data Table 1**). Doublet and low-quality filtering left  
31 166,149 total cells (28,465 single cells and 137,684 single nuclei). The data from both  
32 approaches were integrated, enabling the identification of the canonical cell types found in  
33 WAT, including adipocytes, ASPCs, vascular cells, and immune cells (**Figures 1c, d;**  
34 **Supplementary Table 1**). As expected, adipocytes were found only in the sNuc-seq dataset. The  
35 sNuc-seq data was also enriched for vascular cells and macrophages, likely because collagenase  
36 digestion did not fully dissociate these cell types. Mesothelial cells were not seen in the scRNA-  
37 seq dataset, which did not include visceral tissue. Some of the visceral samples included cells  
38 that appeared to be endometrial in origin (*PRLR*+), likely due to endometriosis. Overall  
39 proportions of adipocytes and ASPCs did not differ between depots, but depot clearly affects the  
40 distribution of cells within these populations (**Extended Data Figure 1a, b, 2a, b, Extended**  
41 **Data Table 2**). In our limited cohort, we could not detect major effects of BMI on cell type  
42 proportions. To assess this finding at larger scale, we utilized our dataset as a reference to  
43 estimate cell type proportions in bulk-RNA sequencing data<sup>12</sup> obtained from the SAT of 331 men  
44 in the METSIM cohort<sup>13</sup>. This deconvolution analysis found that the relative abundance of  
45 adipocytes in that cohort was negatively correlated with BMI, while ASPCs and myeloid cells  
46 were positively correlated (**Figure 1e**).

47

## 48 **A single cell atlas of mouse white adipose tissue**

49 Murine models are commonly used to study adipose tissue biology<sup>14</sup>. We thus sought to  
50 compare mouse and human WAT at the single cell level by performing sNuc-seq on inguinal  
51 (ING, corresponding to human SAT) and perigonadal [PG, epididymal (EPI) in males,  
52 periovarian (POV) in females, corresponding to human VAT] adipose tissue of mice fed either a  
53 chow or high fat diet for 13 weeks (**Figure 2a, b**). After doublet removal and quality filtering,  
54 we considered a total of 197,721 cells (106,469 from PG and 91,252 from ING), identifying all  
55 cell types observed in human WAT (**Figure 2c, d; Supplementary Table 2**) with the addition of  
56 distinct male and female epithelial populations (*Dcdc2a*<sup>+</sup> and *ErbB4*<sup>+</sup>, respectively). The female  
57 population is largely found in ING samples and resembles mammary epithelial cells, while the  
58 male population is almost exclusively found in PG samples, and as noted by others<sup>9</sup> may  
59 represent contaminants from the epididymis and other reproductive structures that are tightly  
60 apposed to fat<sup>15</sup>. In contrast to the human data, cell type abundance in mouse WAT are highly  
61 dependent on body weight with relatively little variation between depots (**Figure 2c** and  
62 **Extended Data Figure 3a, b, Extended Data Table 2**). The proportions of cell types in mouse  
63 adipose tissue after HFD were notably different between male and female mice, which might  
64 reflect a true sex difference, or may reflect that males gain more weight on HFD (**Extended**  
65 **Data Figure 3b**). To compare across species, we used a reference mapping algorithm to assign  
66 each mouse cell to a human cluster and noted a high degree of overall similarity between  
67 annotated mouse clusters and mapped human clusters (**Extended Data Figure 3c**). Similarly, the  
68 proportions of each cell type were roughly similar between humans and chow-fed mice (compare  
69 **Extended Data Figure 2b** to **Extended Data Figure 3b**).

70

## 71 **Analysis of human and mouse stromal-vascular cellular subtypes**

### 72 *Vascular Cells*

73 Subclustering of human vascular cells revealed expected cell types including blood  
74 endothelial clusters that represent arteriolar, stalk, and venular cells, as well as lymphatic  
75 endothelial cells (LECs), pericytes, and two distinct populations of smooth muscle cells (SMCs)  
76 **(Extended Data Figure 4a, b)**. Mouse vascular cells formed similar clusters, but with only one  
77 SMC cluster **(Extended Data Figure 4c, d)**. As expected, reference mapping demonstrated high  
78 similarity between human and mouse vascular subclusters **(Extended Data Figure 4e)**. The  
79 proportions of vascular cells were similar across depots for both mouse and human, although  
80 LECs were to be more common in visceral fat of both species **(Extended Data Figure 4f, g)**.  
81 There was little effect of adiposity on vascular cell populations in the human samples; mice,  
82 however, showed significant changes in vascular cells after high fat feeding, including a lower  
83 proportion of *Dkk2*<sup>+</sup> arteriolar cells and concomitantly higher levels of venular cells. There was  
84 also a reduction in the relative proportion of LECs and increased pericytes on HFD **(Extended**  
85 **Data Figure 4f, g)**.

86

### 87 *Immune Cells*

88 Analysis of human immune cells from scRNA-seq and sNuc-seq samples again revealed  
89 expected cell types, including multiple subpopulations of monocytes, macrophages (*CD14*<sup>+</sup>),  
90 dendritic cells (DCs), B and T lymphocytes, and NK cells (*CD96*<sup>+</sup>), as well as mast cells  
91 (*CPA3*<sup>+</sup>) and neutrophils (*CSF3R*<sup>+</sup>) **(Extended Data Figure 5a, b)**. These subpopulations  
92 resemble known immune cell populations. For example, monocyte subpopulations 1 and 2

93 resemble classical and non-classical monocytes and DC subpopulations 1 and 2 similarly  
94 resemble previously reported *CLEC9A*<sup>+</sup> and *CD1C*<sup>+</sup> populations from blood, respectively<sup>16</sup>.  
95 Lymphocytes also resemble previously reported B cell, T Cell, and NK cell populations from  
96 human WAT, including *CTLA4*<sup>+</sup> hTregs<sup>17</sup>. Examination of the mouse WAT immune  
97 compartment revealed most of the same cell types, although there were notable differences in the  
98 relative abundance of myeloid and lymphoid cells between species (**Extended Data Figure 5c,**  
99 **d**). Human WAT contains somewhat fewer T/NK cells than macrophages/monocytes (~30% vs.  
100 ~60% of recovered immune cells); this imbalance was greatly exaggerated in murine WAT  
101 (macrophages ~90% of recovered immune cells vs. 3% T/NK cells). Because a wealth of data  
102 supports a key role for macrophages/monocytes in adipose biology<sup>18,19</sup>, we separated these cell  
103 types from other immune cells *in silico* for subsequent analysis. Mouse clusters of non-  
104 monocytes/macrophages mapped relatively well to their human counterparts, with some mixing  
105 of T and NK populations (**Extended Data Figure 5e**). Macrophages and monocytes also mapped  
106 well to their general class, but this association often broke down when considering macrophage  
107 subpopulations (**Extended Data Figure 5f**). Thus, mouse cluster mMac3, which comprises the  
108 *Trem2*<sup>+</sup> cells also called “lipid-associated” macrophages<sup>1</sup> maps well to *TREM2*<sup>+</sup> human hMac2  
109 cells, as expected, but hMac2 also associated with every other mouse macrophage subpopulation,  
110 most notably the *Fgf13*<sup>+</sup> mMac1 group (**Extended Data Figure 5f**).

111 The proportion of immune cell populations was similar in human SAT and VAT, with a few  
112 exceptions, such as *PROS1*<sup>+</sup> hMac3 cells which were more abundant in VAT (**Extended Data**  
113 **Figure 6a, e**). In mice, small depot-dependent differences were eclipsed by relatively huge shifts  
114 in response to diet in male mice (**Extended Data Figure 6b, d, f**). Most notably, HFD resulted  
115 in a massive increase in macrophage numbers, primarily in PG, consistent with a large body of

116 prior data<sup>18,21</sup>, (**Extended Data Figure 3c, 6f**). As a proportion of total immune cells, HFD  
117 induced large shifts in mMac1 (down in ING, up in EPI), mMac2 (down in EPI), and *Trem2*<sup>+</sup>  
118 mMac3 (up in ING and EPI) in male mice (**Extended Data Figure 6f**). Reductions in the  
119 proportion of most other immune cell types (e.g., NK cells, T and B lymphocytes, DCs, and  
120 neutrophils) are likely due to the large influx of macrophages, rather than to intrinsic loss of  
121 those specific cell types following HFD (**Extended Data Figure 6b, d, f**). Mast cells increase  
122 proportionally after HFD despite the influence of macrophages, as previously reported<sup>22</sup>. Female  
123 mice exhibit a much less impressive response to HFD, with the only significantly different diet-  
124 related change being a reduction in *Prg4*<sup>+</sup> mMac4 cells (**Extended Data Figure 6f**).

125 Accumulation of adipose tissue macrophages in obesity has also been shown in human WAT,  
126 using a combination of histomorphometry and flow sorting<sup>19,23</sup>. Our data are in general support  
127 of this conclusion, though the magnitude of the effect is significantly less prominent than that  
128 seen in mouse WAT (**Extended Data 2b, 6c, e, f**). The largest change involves hMac3, which is  
129 induced in visceral fat with higher BMI (**Extended Data 6c, e**). We did not observe differential  
130 representation of other immune cell in WAT from subjects with high BMI vs. low BMI.

131

### 132 *Mesothelial cells*

133 Subclustering of mesothelial cells revealed three populations in both human VAT and mouse  
134 PG (**Extended Data Figure 7a-d**). Only sNuc-seq samples were used in this analysis because  
135 our human scRNA-seq data did not include VAT. When mouse mesothelial clusters were  
136 mapped to human clusters, cells were split between human clusters hMes1 and hMes2, with no  
137 cells mapping to hMes3 (**Extended Data Figure 7e**). The proportions of most mesothelial  
138 subpopulations did not vary with obesity or high fat diet, with the exception of hMes1 and



139 hMes2, which were reduced and increased in higher BMIs, respectively. (**Extended Data Figure**  
140 **7f, g**).

141

142 *ASPCs* (see **Supplementary Note 1**)

143 We identified six distinct subpopulations of human ASPCs in subclustered scRNA-seq and  
144 sNuc-seq samples, all of which express the common marker gene *PDGFRA* (**Extended Data**  
145 **Figure 8a, b**). Similarly, we noted six subpopulations in the mouse ASPC data, all of which  
146 were also *Pdgfra*<sup>+</sup> and some of which correspond well with a particular human subpopulation  
147 (**Extended Data Figure 8c-e**). For example, mASPC2 and hASPC2 are both characterized by  
148 high expression of *Aldh1a3/ALDH1A3*, and strongly resemble previously identified early  
149 multipotent progenitor cells that reside in the reticular interstitium of the fat pad<sup>5</sup>. Similarly,  
150 mASPC4 and hASPC4 express *Epha3/EPHA3* and likely represent the anti-adipogenic Areg  
151 population reported by Schwalie et. al.<sup>3</sup>. Seeking to better place our mouse ASPC data into the  
152 overall context of the published literature, we performed reference mapping between our ASPCs  
153 and ASPC populations reported by others<sup>3-6,9</sup> and found general agreement across studies  
154 (**Extended Data Figure 8f**). As mentioned, mASPC2 cells map to the *Dpp4+/Ebf2+* ASPCs  
155 identified by other studies and mASPC1 and mASPC6 map strongly to adipose progenitors,  
156 including the *Icam1*<sup>+</sup> cells identified by Merrick et. al.<sup>5</sup>.

157 Many human and mouse ASPC subclusters showed dependency on diet, depot, or both.  
158 hASPC1, hASPC4, and hASPC5 were more prevalent in SAT than VAT, with increases in SAT  
159 hASPC4 and hASPC5 proportion in subjects with higher BMI (**Extended Data Figure 9a, c, e**).  
160 Conversely, hASPC3 and hASPC6 were more prevalent in VAT. In male mice, early progenitor  
161 cells (mASPC2) were notably more abundant in ING than PG; such depot selectivity was not

162 noted for the analogous hASPC2 in humans. mASPC5 and mASPC6 were more prevalent in EPI  
163 vs ING, although this varied with obesity (e.g., the proportion of mASPC6 cells was greater in  
164 EPI than ING, but only after HFD) (**Extended Data Figure 9b, d, f**). Many of these  
165 observations are consistent with previous findings in adipose biology. For example, HFD has  
166 been shown to increase adipogenesis specifically in PG in mice<sup>24,25</sup>. Our data indicates that pre-  
167 adipocyte subclusters like mASPC6 increase dramatically in response to HFD in PG only. The  
168 loss of early progenitors (mASPC2) in PG with HFD is consistent with conversion of these cells  
169 along the differentiative pathway, i.e., toward mASPC6 (**Extended Data Figure 9b, d, f**). These  
170 patterns are harder to discern in the human samples, which may reflect the fact that patient data  
171 are captured at variable time points after the onset of obesity, whereas the mouse samples are  
172 synchronized over a relatively short time period. Nonetheless, we do observe a VAT-specific  
173 increase in hASPC6 in subjects with high BMI (BMI > 40) (**Extended Data Figures 8e, 9e**).

174

### 175 **Unique subpopulations of human white adipocytes**

176 White adipocytes are generally considered to be monotypic and essentially uniform in  
177 function, although some recent studies have begun to challenge this assumption<sup>8-10,26</sup>. The high  
178 resolution of our data enabled us to find that human white adipocytes cluster into seven  
179 subpopulations with distinct markers (**Figure 3a-b**). We noted strong depot-specific associations  
180 of adipocyte subtypes, with hAd1, hAd3, hAd4, and hAd7 localized primarily to SAT, while  
181 hAd2 and hAd6 were almost exclusively found in VAT. hAd5 represents a smaller population  
182 that is roughly equally distributed between SAT and VAT (**Extended Data Figure 10a-c**). We  
183 also noted a BMI-dependent shift in adipocyte subtype within both depots (**Extended Data**  
184 **Figure 10b, c**). Importantly, all adipocyte subpopulations are present in the majority of subjects,

185 indicating that these subtype designations are generalizable and do not reflect sample-specific  
186 variation (**Extended Data Figure 10c**). Immunohistochemistry (IHC) and/or  
187 immunofluorescence of markers for hAd4, hAd5, hAd6, and hAd7 in human subcutaneous or  
188 visceral adipose tissue identified specific subpopulations of adipocytes at proportions similar to  
189 those seen in the single cell data (**Figure 3c** and **Extended Data Figure 10 d, e**). To examine  
190 whether SAT subtype proportion was influenced by BMI in a larger dataset, we estimated  
191 individual subtype proportions by deconvolution analysis of bulk RNA-seq data from purified  
192 isolated subcutaneous human adipocytes from 43 women (**Figure 3d**). This analysis showed that  
193 clusters hAd4 and hAd7 trend to negative correlation with BMI, aligning with our IHC findings,  
194 while hAd5 proportion is positively correlated with BMI. Visceral adipocytes are absent from  
195 this dataset and so we were unable to assess the prevalence of hAd2 or hAd6 in this cohort,  
196 although IHC of hAd6 marker EBF2 also suggests its prevalence may be positively correlated  
197 with BMI (**Figure 3c**).

198 A critical question is whether individual adipocyte subpopulations have specific functions.  
199 To assess this, we first looked at genes that participate in the major metabolic activities of  
200 adipocytes, including adipokine synthesis and secretion, insulin signaling, lipid handling, and  
201 thermogenesis. All subpopulations expressed these genes, although their relative levels differed.  
202 Thus, the adipokines adiponectin and adipsin (*CFD*) are most highly expressed in hAd3, and  
203 insulin signaling components like *INSR*, *IRS1* and *IRS2* are most highly expressed in hAd5  
204 (**Extended Data Figure 10f**). We next looked more holistically at the data by performing  
205 pathway analysis for markers of each subpopulation (**Supplementary Table 3, Extended Data**  
206 **Figure 10g-m**). Subpopulations hAd1, which accounts for ~40% of SAT adipocyte nuclei, and  
207 hAd2, which accounts for ~60% of VAT adipocyte nuclei, have relatively few specific markers,

208 and the pathways that emerged were similarly unrevealing (**Extended Data Figure 10g, h**).

209 These populations likely represent “basal” subcutaneous or visceral adipocytes, so we therefore

210 focused on subpopulations hAd3-hAd7 for more detailed analysis. hAd3, which comprises ~15%

211 of VAT, was associated with “triglyceride biosynthesis” and included higher expression of

212 *DGAT2*, *SREBF1*, and *PNPLA3* (**Extended Data Figure 10i**). The hAd4 cluster, which makes

213 up ~40% of SAT, expresses the highest levels of several fatty acid desaturases, including

214 *ELOVL5* and *FADS3* (**Extended Data Figure 10j**), which is particularly interesting in light of

215 the insulin-sensitizing role of unsaturated lipokines such as palmitoleate<sup>27</sup>. hAd5 adipocytes

216 comprise a relatively small amount of both SAT and VAT, and besides having the highest

217 expression of several insulin signaling genes, were also characterized by expression of

218 “sphingolipid signaling genes” (**Extended Data Figure 10k**). Both hAd3 and hAd4 express high

219 levels of lipogenic genes, while hAd5 expresses higher levels of lipolysis genes (**Extended Data**

220 **Figure 10f**).

221 We next asked whether cultured human adipocytes retain evidence of subpopulation

222 diversity. To that end, we utilized 57 RNA-seq datasets from human subcutaneous and visceral

223 adipocyte progenitors differentiated *ex vivo* over a 14 day timecourse<sup>28</sup>. Deconvolution analysis

224 revealed that many subpopulations identified *in vivo* were retained in the dish. Furthermore,

225 much of the previously noted depot selectivity was recapitulated, such that the visceral

226 subpopulations hAd2 and hAd6 were significantly more likely to appear in cultured visceral cells

227 and the subcutaneous subpopulation hAd4 was overrepresented in cultured subcutaneous cells

228 (**Extended Data Figure 11a**). Furthermore, because these cultured samples were also subjected

229 to high-content image-based profiling using LipocyteProfiler<sup>28</sup>, we were able to correlate

230 individual subpopulations with image-based features representing morphological and cellular

231 phenotypes including lipid and mitochondrial content. Thus, *ex vivo* differentiated adipocyte  
232 cultures predicted to have high amounts of hAd3, which express high levels of lipogenic genes  
233 and lower levels of lipolytic genes have more overall lipid and larger lipid droplets (**Figure 3e,**  
234 **f**). Conversely, *ex vivo* differentiated adipocyte cultures with high predicted hAd5 content have  
235 less overall lipid and smaller lipid droplets, consistent with higher expression of lipolytic genes  
236 and less lipogenic gene expression (**Extended Data Figure 11b-d**).

237 One particularly interesting adipocyte subpopulation is hAd6, which selectively expresses  
238 genes typically associated with thermogenesis, such as *EBF2*, *ESRRG*, and *PPARGC1A*  
239 (**Extended Data Figure 10I**), a surprising finding given that this population is almost  
240 exclusively visceral (**Figure 3c, Extended Data Figure 10c**). To better understand the  
241 relationship between this subpopulation and visceral adiposity, we looked further into the hAd6  
242 marker *EBF2*, which has previously been identified as a pro-thermogenic transcription factor<sup>29</sup>.  
243 SNPs at the *EBF2* locus are associated with waist-hip ratio (WHR)<sup>30</sup>, which could involve  
244 actions in either SAT or VAT. Interestingly, however, a recent study of GWAS loci associated  
245 with adiposity in specific depots<sup>31</sup> found a common variant 15 kb upstream of *EBF2* that was  
246 associated specifically with VAT (**Extended Data Figure 12a**). Further analysis revealed that  
247 the minor allele of this SNP (MAF = 0.23) was associated with VAT adjusted for BMI and  
248 height (VATadj: beta = 0.062 SD per allele,  $p = 1.0 \times 10^{-12}$ ), but not abdominal subcutaneous  
249 (ASAT) or gluteofemoral (GFAT) depots (ASATadj: beta = -0.018 SD per allele,  $p = 0.03$ ),  
250 GFATadj: beta = -0.020 SD per allele,  $p = 0.02$ , **Extended Data Figure 12b**). We additionally  
251 stratified individuals into either 0, 1, or 2 carriers of the minor allele and observed an additive  
252 trend (G/G median VATadj -0.10 SD, G/A median VATadj = -0.04 SD, A/A median VATadj  
253 0.04 SD; **Extended Data Figure 12c**). Next, we returned to the visceral human adipocytes

254 differentiated *ex vivo*, and found that samples predicted to have a higher proportion of hAd6  
255 adipocytes were characterized by higher mitochondrial intensity and increased expression of  
256 mitochondrial and thermogenic genes (**Extended Data Figure 12d-f**). Finally, our analysis of  
257 hAd6 markers suggested other pathways associated with thermogenesis, including one for “axon  
258 guidance” (**Extended Data Figure 12g**). We could not measure innervation directly using our  
259 data, because the nuclei of innervating sympathetic neurons are located in the spinal ganglia and  
260 not the fat depot itself. Nonetheless, we estimated relative levels of innervation using the  
261 presence of neuron-specific gene expression in the ambient RNA of our visceral sNuc-seq  
262 samples. Indeed, the amount of pan-neuronal markers like *TUBB3* ( $\beta$ III-tubulin) and *UCHL1*  
263 (*PGP9.5*)<sup>32</sup> strongly correlate with hAd6 proportion (**Extended Data Figure 12e**), further  
264 supporting a role for hAd6 as a novel visceral adipocyte subtype with thermogenic potential.

265

### 266 **Adipocytes of mice and humans show critical similarities and differences**

267 Subclustering mouse adipocytes revealed six subpopulations (**Figure 3g, h**). Unlike human  
268 adipocytes, mouse adipocyte subtypes exhibit little depot enrichment, especially on chow diet  
269 (**Extended Data Figure 13a-c**). There was strong diet-dependency, however, as relative  
270 proportions of mAd1 and mAd3 were reduced after HFD, while the opposite was noted for  
271 mAd4 and mAd5 (**Extended Data Figure 13b, c**). In contrast to the relatively good cross-  
272 species concordance between immune cells, vascular cells, and ASCs, mouse adipocytes do not  
273 map cleanly onto human adipocyte subpopulations. The majority of murine ING adipocytes map  
274 most closely to hAd1, while PG adipocytes map to hAd6, with some mapping to hAd2.  
275 (**Extended Data Figure 13d-f**).

276 As in the human, genes associated with major adipocyte functions showed some  
277 subpopulation selectivity. For example, lipogenesis genes were highest in HFD-induced  
278 population mAd5 (**Extended Data Figure 13c, g**). More detailed pathway analysis on mouse  
279 adipocyte subpopulations (**Supplementary Table 3**) showed that the chow-associated clusters  
280 mAd1-3 were notably enriched in metabolic pathways, particularly those involved in lipid  
281 handling (**Extended Data Figure 13h-j**). The HFD-associated clusters mAd4-6, on the other  
282 hand, were linked to pathways like “HIF-1 signaling”, “actin cytoskeleton”, and “NF-κB  
283 signaling” (**Extended Data Figure 13k-n**), consistent with the known roles of hypoxia,  
284 cytoskeletal remodeling, and inflammation in HFD-induced adipose dysfunction and insulin  
285 resistance<sup>23-25</sup>.

286 Our data allows us to address an important question: are diet-induced changes in gene  
287 expression at the population level shared among subpopulations or do they reflect a change in the  
288 relative proportion of these subpopulations? To assess this, we examined the twenty most  
289 positively and negatively regulated genes from a TRAP-based RNA-seq experiment in white  
290 adipocytes from mice fed chow or high fat diet<sup>34</sup> (**Extended Data Figure 14a**). We noted that  
291 some genes, such as *Cyp2e1*, and *Fam13a*, exhibit elevated expression in chow adipocytes in  
292 virtually all subpopulations, even those clusters that are selective for HFD (**Extended Data**  
293 **Figure 14b**). However, while the chow-associated gene *Cfd* is reduced in all populations with  
294 HFD, expression seems largely driven by the mAd3 population which has the highest expression  
295 of *Cfd* and decreases in abundance with HFD (**Extended Data Figure 13b,c, 14b**). *Sept9*,  
296 *Cdkn1a*, and *Fgfl3* show increased gene expression after HFD across almost all subpopulations  
297 while other HFD-induced genes (e.g., *Slc5a7* and *Dclk1*) increase their expression after HFD in  
298 the chow-associated clusters (mAd1-4) but not in the HFD-associated clusters mAd5-7

299 **(Extended Data Figure 14b)**. Thus, diet-dependent expression changes reflect both alterations  
300 across all clusters and the emergence or disappearance of distinct populations.

301 Finally, we were somewhat surprised that we did not see a murine population that could be  
302 clearly delineated as thermogenic. Such cells have been noted by others in WAT, even at room  
303 temperature<sup>36</sup>. Notably, the distribution of beige adipocytes is not uniform in ING, but tends to  
304 be densest close to the inguinal lymph node (LN)<sup>37</sup>. To avoid contamination by LN cells, we  
305 excised the node with a fairly wide margin, and it is possible that our samples were thus de-  
306 enriched for beige adipocytes. Nonetheless, when we considered the chow fed samples  
307 independently, mAd1 split into three clusters **(Extended Data Figure 15a, b)**. Two of these  
308 clusters, mAd1B and mAd1C, were recognizable as thermogenic beige adipocytes, with  
309 relatively high expression of *Prdm16* and *Ppargc1a* in mAd1B and even higher expression of  
310 these genes, as well as expression of *Ucp1* and *Cidea* in mAd1C **(Extended Data Figure 15c)**.  
311 As expected, the thermogenic mAd1B and mAd1C subpopulations were enriched in ING vs. PG  
312 samples **(Extended Data Figure 15d, e)** and suggest HFD-induced transcriptional variability  
313 masks these subtype designations.

314

### 315 **Exploration of cell-cell interactions within the adipose niche**

316 The functions of WAT are known to be coordinated by neural and hormonal cues from  
317 outside the fat pad<sup>38</sup>. There is growing appreciation, however, that intercellular communication  
318 within the depot is also critical for the WAT response to overnutrition and other stressors<sup>39</sup>. In  
319 particular, attention has focused on cross-talk between adipocytes and immune cells (especially  
320 macrophages) in the context of obesity<sup>40</sup>. To assess potential interactions between all identified  
321 cell types in different depots and at different body mass, we utilized CellPhoneDB<sup>41</sup>, which



322 utilizes information about the expression of ligand-receptor pairs to estimate cell type  
323 communication (**Supplementary Table 4, Supplementary Table 5**). As expected, we detected  
324 increased potential communication between human adipocytes and macrophages in high BMI vs.  
325 low BMI subjects; of 84 potential interactions identified between human adipocytes and  
326 macrophages, 40 (48%) were specific for high BMI subjects, while only 3 (4%) were specific for  
327 low BMI subjects (**Figure 4a, Extended Data Figure 16a, d**). Notably, obesity was also  
328 associated with robustly increased expression of genes encoding ligand-receptor pairs between  
329 adipocytes and many non-immune cell types, including blood and lymphatic endothelial cells,  
330 vascular SMCs, pericytes, and ASPCs (**Figure 4a, b, Extended Data Figure 16a, d**). For  
331 example, of 145 potential interactions identified between human adipocytes and endothelial  
332 cells, 65 (45%) were specific for high BMI subjects, while only 6 (4%) were specific for low  
333 BMI subjects (**Extended Data Figure 16d**). Potential interactions between these cell types are  
334 frequently bidirectional, and receptors are often expressed on multiple cell types, suggesting  
335 networks of communication (**Figure 4b, Extended Data Figure 16e**). We also noted differential  
336 expression of ligands and receptors within human adipocyte subpopulations, lending further  
337 support to the idea that they carry out distinct functions (**Extended Data Figure 16b**). The  
338 specific interactions upregulated during obesity suggest that adipocytes play a significant role in  
339 obesity-related adipose tissue remodeling. For example, adipocyte expression of angiogenic  
340 factors like *JAG1* and *VEGFC* is increased in the obese state, as is true of the expression of their  
341 receptors (e.g., *NOTCH3* and *KDR*) on endothelial cells, consistent with obesity-associated  
342 induction of angiogenesis by adipocytes<sup>42</sup> (**Figure 4b, Supplementary Table 6**).

343 Analysis of the mouse data yielded similar results, as HFD increased the intensity of ligand-  
344 receptor pair expression, with the most prominent interactions again occurring between non-

345 immune cell types, especially between ASPCs and adipocytes, pericytes, and SMCs (**Extended**  
346 **Data Figure 16c**). Interactions between WAT cell types include several that have been studied,  
347 such as the effect of the adipokine leptin on endothelial cells via LEPR<sup>43</sup>, and the actions of  
348 TGFBI on adipose fibrosis via TGFBR1<sup>34</sup>. The majority of these interactions, however, are  
349 unstudied in the context of WAT function and dysfunction.

350 In human samples, most interactions between adipocytes and endothelial cells were shared  
351 between SAT and VAT (61%), but of those interactions not shared between depots, the majority  
352 were seen in SAT (31% vs. 8% specific for VAT). This same pattern was seen when looking at  
353 adipocyte-ASPC interactions (38% SAT-specific vs. 11% VAT-specific), and adipocyte-  
354 macrophage interactions (27% SAT-specific vs. 12% VAT-specific). In mice, we noted a more  
355 even split between ING- and EPI-specific interactions (e.g., 13% ING-specific vs. 12% EPI-  
356 specific adipocyte-endothelial interactions). Adipose niche interactions were only modestly  
357 conserved between mouse and human. (**Extended Data Figure 16d**).

### 358 **Relationships between WAT cell types and human disease**

359 Adiposity is associated with a wide range of metabolic diseases and traits, and GWAS  
360 studies have suggested a specific link between WAT and coronary artery disease (CAD), BMI-  
361 adjusted T2D, dyslipidemia, and BMI-adjusted waist-hip ratio (WHR, a measure of body fat  
362 distribution)<sup>44-46</sup>. To determine which specific cell types in WAT are likely to mediate these  
363 associations, we employed CELLECT, a method for integrating scRNA-seq and sNuc-seq data  
364 with GWAS<sup>47</sup>. As expected, Type 1 Diabetes (T1D) was significantly associated with B and T  
365 lymphocytes and NK cells, consistent with the known autoimmune basis of that disease (**Figure**  
366 **4c**). No WAT cell type associated with BMI, as expected given the strong neuronal basis of body  
367 weight regulation<sup>48</sup>. The strongest phenotypic association for white adipocytes was with BMI-

368 adjusted WHR, and associations approaching significance were also noted between adipocytes  
369 and HDL and T2D (**Figure 4c, Supplementary Table 7**).

370 Because all adipocyte subpopulations were significantly associated with WHR (**Figure 4d**),  
371 we looked for adipocyte genes responsible for the association with WHR that are not specific to  
372 any particular subpopulation. One such gene is *PPARG*, which is highly expressed in all  
373 adipocytes (**Extended Data Figure 17a**). Data from the METSIM cohort indicates a strong  
374 inverse relationship between WHR and *PPARG* levels in whole WAT (**Extended Data Figure**  
375 **17b**). Unfortunately, WHR was not recorded in the cohort used to generate our floated human  
376 adipocytes. WHR is, however, highly correlated with HOMA-IR<sup>11</sup>, and we found that *PPARG*  
377 levels showed a strong inverse relationship with HOMA-IR in both the METSIM cohort and in  
378 our floated adipocytes (**Extended Data Figure 17c, d**). Furthermore, SNPs in the *PPARG* gene  
379 that are associated with BMI-adjusted WHR<sup>30</sup> are also significantly associated with *PPARG*  
380 mRNA levels and HOMA-IR in our floated adipocyte cohort (**Extended Data Figure 17e-h**).

381 Adipocytes were also the cell type most likely to mediate the association of WAT with T2D,  
382 with the strongest association specifically with hAd7 (**Figure 4d**). To further investigate the  
383 association between hAd7 and T2D, we took our deconvolved bulk RNA-seq data from floated  
384 human adipocytes and plotted the abundance of hAd7 as a function of HOMA-IR. This revealed  
385 that hAd7 shows significant inverse correlation with insulin resistance (**Figure 4e**). We then  
386 searched for specific hAd7 marker genes that exhibit this same relationship with HOMA-IR, and  
387 identified several, including *AGMO*, *ALPK3*, *FHOD3*, and *LIN7A* (**Figure 4f, g**). Of note,  
388 *AGMO* (also called *TMEM195*) has emerged as a candidate locus in T2D GWAS<sup>49,50</sup>. Taken  
389 together, our data suggest that hAd7 may have an outsized influence on the risk of T2D, despite  
390 representing only ~1% of human adipocytes.

391        Additionally, although adipocytes did not meet genome-wide significance for an association  
392 with LDL, we were struck by the near significant relationship between LDL and hAd1, and to a  
393 lesser extent, hAd4 (**Figure 4c, d**). We noted several genes that were selective for hAd1 and/  
394 hAd4, including *NRCAM*, *PEMT*, *PCDH7*, and *VGLL3*, all of which showed a strong positive  
395 relationship between expression and LDL levels in our floated adipocyte cohort (**Extended Data**  
396 **Figure 17i, j**)

397        We also performed CELLECT using the mouse data and noted associations between BMI-  
398 adjusted WHR and murine adipocytes (particularly mAd1, mAd3, and mAd6), as well as pre-  
399 adipocytes (especially mASPC2) (**Extended Data Figure 18a-c**). This suggests that WHR may  
400 be determined in large part by alterations in adipocyte differentiation, a hypothesis consistent  
401 with the *PPARG* data above, and with independent studies of different WHR genes<sup>51</sup>. HDL and  
402 TG levels are also associated with mouse white adipocyte gene expression (**Extended Data**  
403 **Figure 18a-c**).

404

## 405 **Discussion**

406        Here, we present a comprehensive atlas of human and mouse WAT across depot and  
407 nutritional state. Our analysis reveals a rich array of cell types, including blood and lymphatic  
408 vascular cells, immune cells, and ASPCs, in addition to adipocytes. These cell types are grossly  
409 similar across species, but differ more profoundly when cellular subpopulations are explored. It  
410 is tempting to attribute these subpopulation differences to divergence across 65 million years of  
411 evolution, but other factors also need to be considered. For example, the human samples were  
412 collected after a fast, while the mice were harvested after *ad libitum* feeding, which might be  
413 expected to cause some differences in cell state related to insulin signaling or related pathways.

414 Ongoing studies are focused on addressing potential effects of fasting/feeding on WAT  
415 composition.

416 Our dataset reveals subpopulations of human white adipocytes that are associated with a  
417 range of adipocyte functions, from lipolysis and lipogenesis to thermogenesis, as well as with  
418 phenotypes such as BMI, WHR, and T2D. The single cell resolution of our dataset enables the  
419 identification of heterogeneity that cannot be appreciated by bulk RNA sequencing, such as a  
420 potentially visceral thermogenic subpopulation (hAd6), and a rare subpopulation associated with  
421 T2DM (hAd7). Our dataset provides a rich resource to identify other disease-associated cell  
422 types and to better interpret GWAS studies of metabolic phenotypes.

423 Overall, our data highlight a central role for adipocytes in the local regulation of the adipose  
424 depot as well as in systemic physiology. We additionally provide a framework for mouse-human  
425 comparison in studies of adipose tissue that will be an important resource for groups hoping to  
426 translate murine findings to human treatments. These data provide a lens of unprecedented acuity  
427 that better informs our understanding of WAT biology and enables a deeper exploration of the  
428 role of adipose tissue in health and disease.

## REFERENCES

- 429 1. Rosen, E. D. & Spiegelman, B. M. What We Talk About When We Talk About Fat. *Cell* **156**,  
430 20–44 (2014).
- 431 2. Kahn, S. E., Hull, R. L. & Utzschneider, K. M. Mechanisms linking obesity to insulin  
432 resistance and type 2 diabetes. *Nature* **444**, 840–846 (2006).
- 433 3. Schwalie, P. C. *et al.* A stromal cell population that inhibits adipogenesis in mammalian fat  
434 depots. *Nature* **559**, 103–108 (2018).
- 435 4. Burl, R. B. *et al.* Deconstructing Adipogenesis Induced by  $\beta$ 3-Adrenergic Receptor Activation  
436 with Single-Cell Expression Profiling. *Cell Metab.* **28**, 300-309.e4 (2018).
- 437 5. Merrick, D. *et al.* Identification of a mesenchymal progenitor cell hierarchy in adipose tissue.  
438 *Science* **364**, (2019).
- 439 6. Hepler, C. *et al.* Identification of functionally distinct fibro-inflammatory and adipogenic  
440 stromal subpopulations in visceral adipose tissue of adult mice. *eLife* **7**, e39636 (2018).
- 441 7. Vijay, J. *et al.* Single-cell analysis of human adipose tissue identifies depot- and disease-  
442 specific cell types. *Nat. Metab.* **2**, 97–109 (2020).
- 443 8. Rajbhandari, P. *et al.* Single cell analysis reveals immune cell–adipocyte crosstalk regulating  
444 the transcription of thermogenic adipocytes. *eLife* **8**, e49501 (2019).
- 445 9. Sárvári, A. K. *et al.* Plasticity of Epididymal Adipose Tissue in Response to Diet-Induced  
446 Obesity at Single-Nucleus Resolution. *Cell Metab.* **33**, 437-453.e5 (2021).
- 447 10. Sun, W. *et al.* snRNA-seq reveals a subpopulation of adipocytes that regulates  
448 thermogenesis. *Nature* **587**, 98–102 (2020).

- 449 11. Benites-Zapata, V. A. *et al.* High waist-to-hip ratio levels are associated with insulin  
450 resistance markers in normal-weight women. *Diabetes Metab. Syndr. Clin. Res. Rev.* **13**, 636–  
451 642 (2019).
- 452 12. Wang, X., Park, J., Susztak, K., Zhang, N. R. & Li, M. Bulk tissue cell type  
453 deconvolution with multi-subject single-cell expression reference. *Nat. Commun.* **10**, 380  
454 (2019).
- 455 13. Raulerson, C. K. *et al.* Adipose Tissue Gene Expression Associations Reveal Hundreds  
456 of Candidate Genes for Cardiometabolic Traits. *Am. J. Hum. Genet.* **105**, 773–787 (2019).
- 457 14. Blüher, M. Transgenic animal models for the study of adipose tissue biology. *Best Pract.*  
458 *Res. Clin. Endocrinol. Metab.* **19**, 605–623 (2005).
- 459 15. An atlas of cell types in the mouse epididymis and vas deferens | eLife.  
460 <https://elifesciences.org/articles/55474>.
- 461 16. Villani, A.-C. *et al.* Single-cell RNA-seq reveals new types of human blood dendritic  
462 cells, monocytes, and progenitors. *Science* **356**, (2017).
- 463 17. Hildreth, A. D. *et al.* Single-cell sequencing of human white adipose tissue identifies new  
464 cell states in health and obesity. *Nat. Immunol.* 1–15 (2021) doi:10.1038/s41590-021-00922-4.
- 465 18. Suganami, T. & Ogawa, Y. Adipose tissue macrophages: their role in adipose tissue  
466 remodeling. *J. Leukoc. Biol.* **88**, 33–39 (2010).
- 467 19. Weisberg, S. P. *et al.* Obesity is associated with macrophage accumulation in adipose  
468 tissue. *J. Clin. Invest.* **112**, 1796–1808 (2003).
- 469 20. Jaitin, D. A. *et al.* Lipid-Associated Macrophages Control Metabolic Homeostasis in a  
470 Trem2-Dependent Manner. *Cell* **178**, 686-698.e14 (2019).

- 471 21. Reilly, S. M. & Saltiel, A. R. Adapting to obesity with adipose tissue inflammation. *Nat.*  
472 *Rev. Endocrinol.* **13**, 633–643 (2017).
- 473 22. Shi, M. & Shi, G.-P. Different Roles of Mast Cells in Obesity and Diabetes: Lessons  
474 from Experimental Animals and Humans. *Front. Immunol.* **3**, 7 (2012).
- 475 23. Xu, H. *et al.* Chronic inflammation in fat plays a crucial role in the development of  
476 obesity-related insulin resistance. *J. Clin. Invest.* **112**, 1821–1830 (2003).
- 477 24. Wang, Q. A., Tao, C., Gupta, R. K. & Scherer, P. E. Tracking adipogenesis during white  
478 adipose tissue development, expansion and regeneration. *Nat. Med.* **19**, 1338–1344 (2013).
- 479 25. Jeffery, E., Church, C. D., Holtrup, B., Colman, L. & Rodeheffer, M. S. Rapid Depot-  
480 Specific Activation of Adipocyte Precursor Cells at the Onset of Obesity. *Nat. Cell Biol.* **17**,  
481 376–385 (2015).
- 482 26. Bäckdahl, J. *et al.* Spatial mapping reveals human adipocyte subpopulations with distinct  
483 sensitivities to insulin. *Cell Metab.* **33**, 1869-1882.e6 (2021).
- 484 27. Stefan, N. *et al.* Circulating Palmitoleate Strongly and Independently Predicts Insulin  
485 Sensitivity in Humans. *Diabetes Care* **33**, 405–407 (2010).
- 486 28. Laber, S. *et al.* *Discovering cellular programs of intrinsic and extrinsic drivers of*  
487 *metabolic traits using LipocyteProfiler*. 2021.07.17.452050  
488 <https://www.biorxiv.org/content/10.1101/2021.07.17.452050v1> (2021)  
489 doi:10.1101/2021.07.17.452050.
- 490 29. Rajakumari, S. *et al.* EBF2 determines and maintains brown adipocyte identity. *Cell*  
491 *Metab.* **17**, 562–574 (2013).



- 492 30. Pulit, S. L. *et al.* Meta-analysis of genome-wide association studies for body fat  
493 distribution in 694 649 individuals of European ancestry. *Hum. Mol. Genet.* **28**, 166–174  
494 (2019).
- 495 31. Agrawal, S. *et al.* *Inherited basis of visceral, abdominal subcutaneous and gluteofemoral*  
496 *fat depots.* 2021.08.24.21262564  
497 <https://www.medrxiv.org/content/10.1101/2021.08.24.21262564v1> (2021)  
498 doi:10.1101/2021.08.24.21262564.
- 499 32. Willows, J. W. *et al.* Visualization and analysis of whole depot adipose tissue neural  
500 innervation. *iScience* **24**, 103127 (2021).
- 501 33. Sun, K., Halberg, N., Khan, M., Magalang, U. J. & Scherer, P. E. Selective Inhibition of  
502 Hypoxia-Inducible Factor 1 $\alpha$  Ameliorates Adipose Tissue Dysfunction. *Mol. Cell. Biol.* **33**,  
503 904–917 (2013).
- 504 34. Roh, H. C. *et al.* Adipocytes fail to maintain cellular identity during obesity due to  
505 reduced PPAR $\gamma$  activity and elevated TGF $\beta$ -SMAD signaling. *Mol. Metab.* **42**, 101086  
506 (2020).
- 507 35. Chiang, S.-H. *et al.* The protein kinase IKKepsilon regulates energy balance in obese  
508 mice. *Cell* **138**, 961–975 (2009).
- 509 36. Park, J. *et al.* Progenitor-like characteristics in a subgroup of UCP1+ cells within white  
510 adipose tissue. *Dev. Cell* **56**, 985-999.e4 (2021).
- 511 37. Chi, J. *et al.* Three-Dimensional Adipose Tissue Imaging Reveals Regional Variation in  
512 Beige Fat Biogenesis and PRDM16-Dependent Sympathetic Neurite Density. *Cell Metab.* **27**,  
513 226-236.e3 (2018).

- 514 38. Priest, C. & Tontonoz, P. Inter-organ cross-talk in metabolic syndrome. *Nat. Metab.* **1**,  
515 1177–1188 (2019).
- 516 39. Schling, P. & Löffler, G. Cross talk between adipose tissue cells: impact on  
517 pathophysiology. *News Physiol. Sci. Int. J. Physiol. Prod. Jointly Int. Union Physiol. Sci. Am.*  
518 *Physiol. Soc.* **17**, 99–104 (2002).
- 519 40. Kane, H. & Lynch, L. Innate Immune Control of Adipose Tissue Homeostasis. *Trends*  
520 *Immunol.* **40**, 857–872 (2019).
- 521 41. Efremova, M., Vento-Tormo, M., Teichmann, S. A. & Vento-Tormo, R. CellPhoneDB:  
522 inferring cell-cell communication from combined expression of multi-subunit ligand-receptor  
523 complexes. *Nat. Protoc.* **15**, 1484–1506 (2020).
- 524 42. Cao, Y. Angiogenesis and vascular functions in modulation of obesity, adipose  
525 metabolism, and insulin sensitivity. *Cell Metab.* **18**, 478–489 (2013).
- 526 43. Hubert, A. *et al.* Selective Deletion of Leptin Signaling in Endothelial Cells Enhances  
527 Neointima Formation and Phenocopies the Vascular Effects of Diet-Induced Obesity in Mice.  
528 *Arterioscler. Thromb. Vasc. Biol.* **37**, 1683–1697 (2017).
- 529 44. Scott, R. A. *et al.* An Expanded Genome-Wide Association Study of Type 2 Diabetes in  
530 Europeans. *Diabetes* **66**, 2888–2902 (2017).
- 531 45. Shungin, D. *et al.* New genetic loci link adipose and insulin biology to body fat  
532 distribution. *Nature* **518**, 187–196 (2015).
- 533 46. Huang, L. O. *et al.* Genome-wide discovery of genetic loci that uncouple excess adiposity  
534 from its comorbidities. *Nat. Metab.* **3**, 228–243 (2021).
- 535 47. Timshel, P. N., Thompson, J. J. & Pers, T. H. Genetic mapping of etiologic brain cell  
536 types for obesity. *eLife* **9**, e55851 (2020).

- 537 48. O’Rahilly, S. & Farooqi, I. S. Human obesity as a heritable disorder of the central control  
538 of energy balance | *International Journal of Obesity*.  
539 <https://www.nature.com/articles/ijo2008239>.
- 540 49. Sailer, S., Keller, M. A., Werner, E. R. & Watschinger, K. The Emerging Physiological  
541 Role of AGMO 10 Years after Its Gene Identification. *Life Basel Switz.* **11**, (2021).
- 542 50. Dupuis, J. *et al.* New genetic loci implicated in fasting glucose homeostasis and their  
543 impact on type 2 diabetes risk. *Nat. Genet.* **42**, 105–116 (2010).
- 544 51. Loh, N. Y. *et al.* RSPO3 impacts body fat distribution and regulates adipose cell biology  
545 in vitro. *Nat. Commun.* **11**, 2797 (2020).

## FIGURES AND FIGURE LEGENDS



546 **Fig. 1. A single cell atlas of human white adipose tissue. a**, Schematic of workflows for  
 547 scRNA-seq and sNuc-seq of human WAT. **b**, Graphical representation of the cohorts for both  
 548 studies. Only the sNuc-seq cohort contains VAT. **c**, UMAP projection of all 166,129 sequenced  
 549 human cells split by cohort. **d**, Marker genes for each cell population in the human WAT dataset.  
 550 **e**, Estimated cell type proportions in bulk RNA sequencing data of subcutaneous adipose tissue  
 551 from 331 individuals from the METSIM cohort calculated using sNuc-seq data as reference.

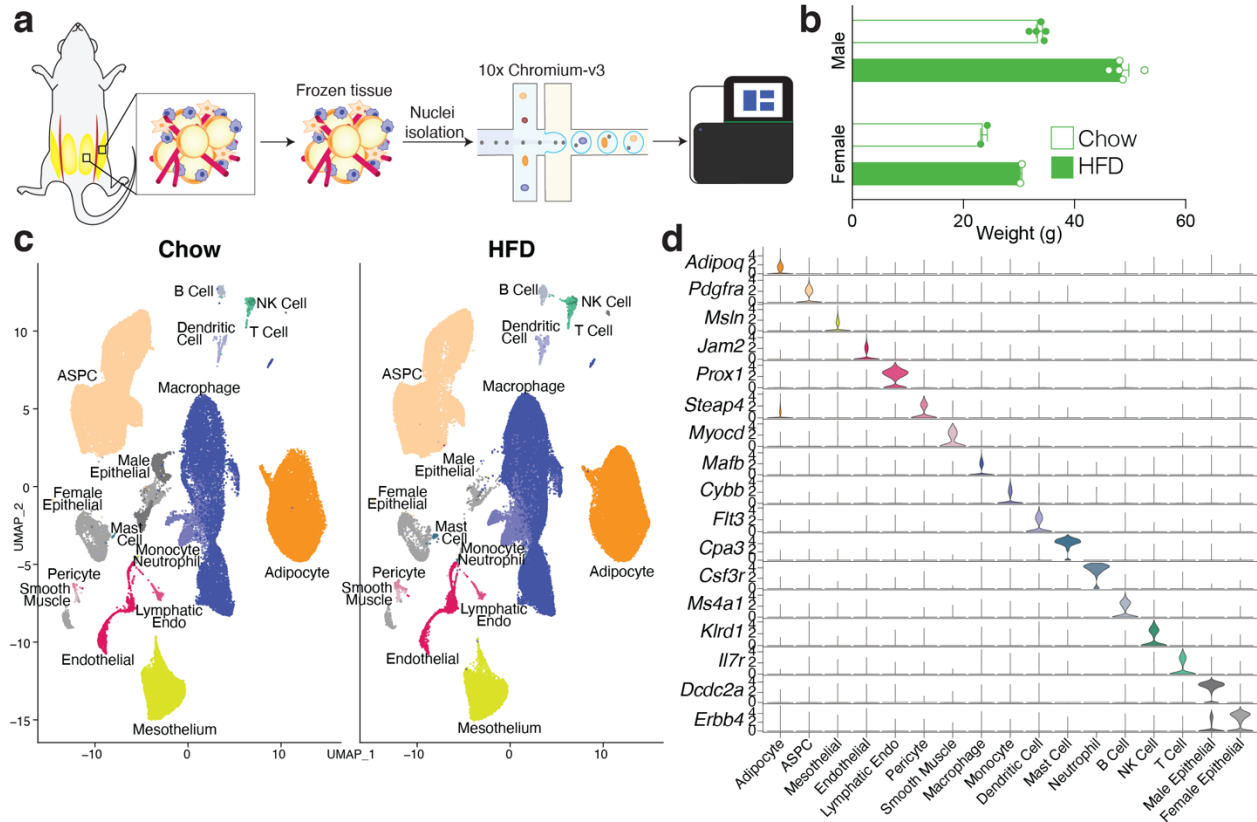
552 Vascular cells include endothelial, lymphatic endothelial, pericytes, and smooth muscle cells.

553 Myeloid immune includes macrophages, monocytes, dendritic cells, mast cells and neutrophils,

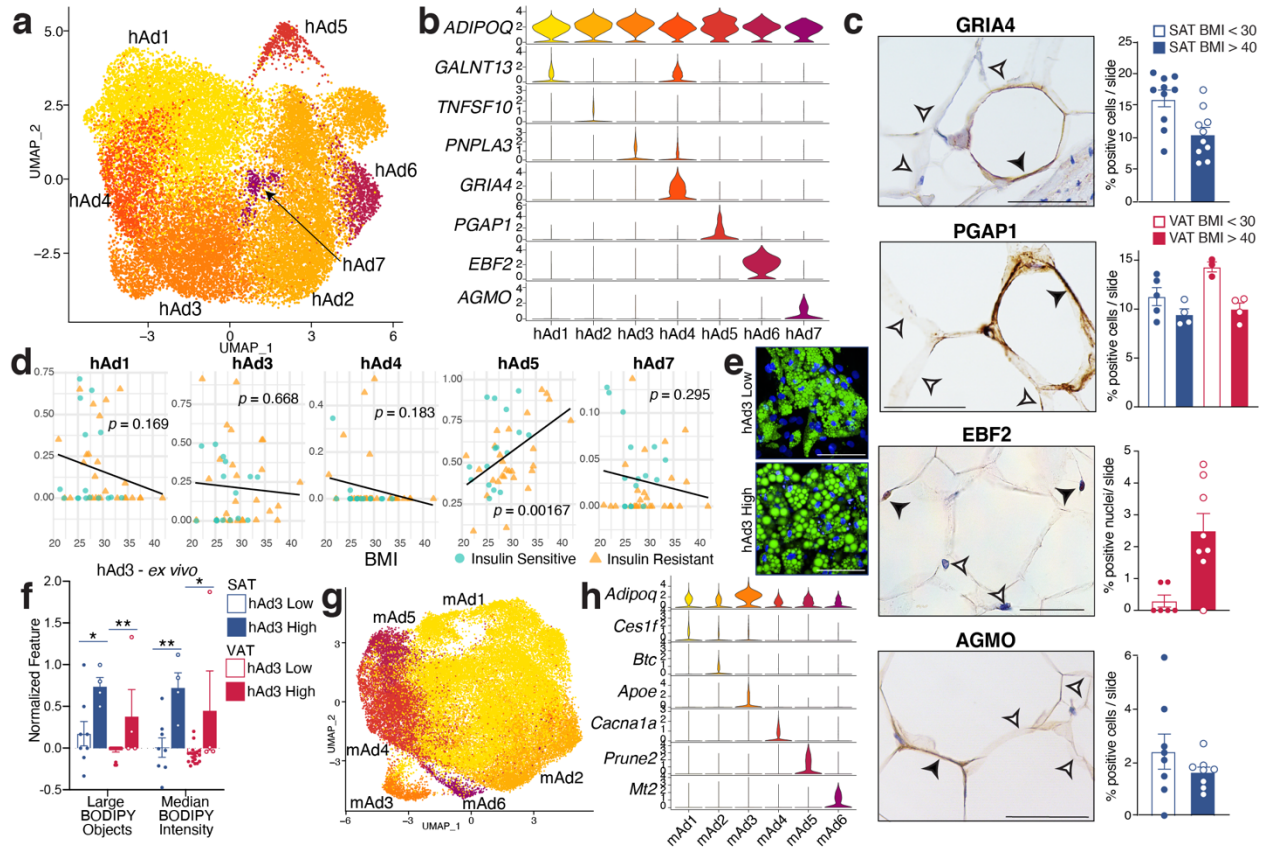
554 and lymphoid immune includes B cells, NK cells, and T cells. For lines of best fit: Adipocytes  $R^2$

555 = 0.031, ASPCs  $R^2 = 0.034$ , Vascular  $R^2 = 0.076$ , Myeloid Immune  $R^2 = 0.13$ , Lymphoid

556 Immune  $R^2 = 0.0049$ .



557 **Fig. 2. A single cell atlas of mouse white adipose tissue.** **a**, Schematic of workflow for sNuc-  
 558 seq of mouse ING and EPI adipose tissue. **b**, Body weight of chow and high fat fed animals. **c**,  
 559 UMAP projection of all 197,721 sequenced mouse cells split by diet. **d**, Marker genes for each  
 560 cell population in the mouse WAT dataset.

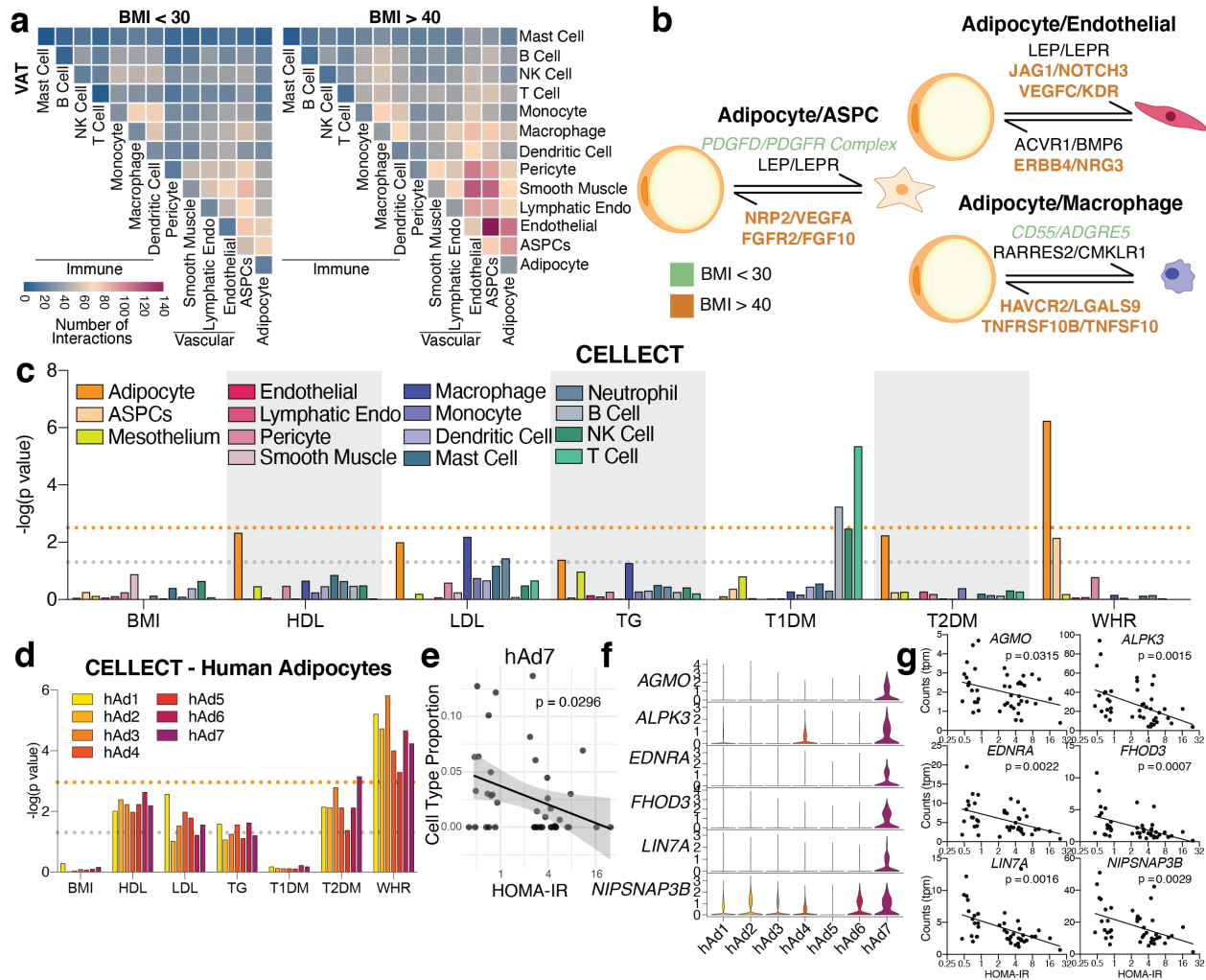


561 **Fig. 3. Subclustering of human and mouse adipocytes reveals multiple distinct populations**

562 **that vary across depot and diet. a**, UMAP projection of clusters formed by 25,871 human  
 563 white adipocytes. **b**, Expression of adipocyte marker *ADIPOQ* as well as specific marker genes  
 564 for each adipocyte subpopulation. **c**, IHC for marker genes of adipocyte subpopulations hAd4,  
 565 hAd5, hAd6, and hAd7 in human adipose tissue and quantification of percentage of positive  
 566 adipocytes per slide in lean and obese individuals (GRIA4: 5 lean, 5 obese, 2 slides per person;  
 567 PGAP1: 5 lean SAT, 4 obese SAT, 3 lean VAT, 4 obese VAT, 1 slide per person; EBF2: 3 lean,  
 568 4 obese, 2 slides per person; AGMO: 4 lean, 4 obese, 2 slides per person). Scale bars are 25  $\mu$ m  
 569 for GRIA4, EBF2, and AGMO, 20  $\mu$ m for PGAP1. **d**, Estimated proportions of adipocyte  
 570 subpopulations in bulk RNA sequencing data of enzymatically isolated subcutaneous adipocytes  
 571 from 43 individuals plotted against subject BMI. **e**, Representative images of *ex vivo*

572 differentiated human subcutaneous adipocytes predicted to have a low or high amount of hAd3  
573 cells based on deconvolution of bulk RNA sequencing data. Green represents BODIPY staining,  
574 blue represents Hoechst staining. Scale bars are 100  $\mu\text{m}$ . **f**, Normalized count of BODIPY-  
575 related features in human subcutaneous and visceral adipocytes differentiated *ex vivo* and  
576 stratified into low and high hAd3-containing populations. **g**, UMAP projection of clusters formed  
577 by 39,934 mouse white adipocytes. **h**, Expression of adipocyte marker *Adipoq* as well as specific  
578 marker genes for each mouse adipocyte subpopulation. For bar graphs, error bars represent  
579 standard error of the mean (SEM), \*,  $p < 0.5$ , \*\*,  $p < 0.1$ . For lines of best fit: hAd1  $R^2 = 0.046$ ,  
580 hAd3  $R^2 = 0.0045$ , hAd4  $R^2 = 0.043$ , hAd5  $R^2 = 0.22$ , hAd1  $R^2 = 0.027$ .





581 **Fig. 4. Extensive cell-cell interactions in WAT and associations with human disease traits.**  
 582 **a**, Heatmap showing number of significant interactions identified between cell types in VAT of  
 583 low (<30) and high (>40) BMI individuals as determined by CellphoneDB. **b**, Selected  
 584 interactions between adipocytes and ASPCs, endothelial cells, and macrophages identified using  
 585 CellphoneDB; orange and green indicate interactions that are significant only in BMI > 40 or  
 586 only in BMI >30, respectively. **c**, CELLECT  $p$  values of the association between cell types in the  
 587 human adipose sNuc-seq dataset with GWAS studies. The grey line represents  $p = 0.05$  and the  
 588 orange line represents significant p value after Bonferroni adjustment ( $p = 0.003$ ), based on  
 589 number of cell types queried. Both T2D and WHR were BMI-adjusted. **d**, CELLECT  $p$  values

590 for adipocyte subpopulations. The grey line represents  $p = 0.05$  and the orange line represents  
591 significant  $p$  value after Bonferroni adjustment ( $p = 0.001$ ), based on all cell subtypes queried. **e**,  
592 Estimated cell type proportion of hAd7 in bulk RNA-seq data of enzymatically isolated  
593 subcutaneous adipocytes from 43 individuals plotted against HOMA-IR. For line of best fit,  $R^2 =$   
594 0.11. **f-g**, Expression of hAd7 marker genes negatively correlated with HOMA-IR in human  
595 adipocyte subpopulations (**f**) and bulk RNA sequencing data of human adipocytes (**g**).

596

## 597 **METHODS**

### 598 **Collection of human adipose tissue samples.**

#### 599 *Drop-Seq and Floated adipocyte bulk RNA-seq*

600 Subcutaneous adipose tissue was collected under Beth Israel Deaconess Medical Center  
601 Committee on Clinical Investigations IRB 2011P000079. Potential subjects were recruited in a  
602 consecutive fashion, as scheduling permitted, from the plastic surgery operating room rosters at  
603 Beth Israel Deaconess Medical Center. Male and female subjects over the age of 18 undergoing  
604 elective plastic surgery procedures and free of other acute medical conditions were included and  
605 provided written informed consent preoperatively. Excess adipose tissue from the surgical site  
606 was collected at the discretion of the surgeon during the normal course of the procedure. Subjects  
607 with a diagnosis of diabetes, or taking insulin-sensitizing medications such as thiazolidinediones  
608 or metformin, chromatin-modifying enzymes such as valproic acid, anti-retroviral medications,  
609 or drugs known to induce insulin resistance such as mTOR inhibitors or systemic steroid  
610 medications, were excluded.

611

#### 612 *sNuc-Seq*

613 Subcutaneous and visceral adipose tissue was collected under BIDMC Committee on Clinical  
614 Investigations IRB 2011P000079 and University of Pittsburgh Medical Center STUDY  
615 19010309. At BIDMC, potential subjects were recruited in a consecutive fashion, as scheduling  
616 permitted, from the gynecological, vascular, and general surgery rosters. Male and female  
617 subjects over the age of 18 undergoing plastic surgery (panniculectomy, thighplasty or deep  
618 inferior epigastric perforators), gynecological surgery (total abdominal hysterectomy and  
619 bilateral salpingo-oophorectomy) or general surgery (cholecystectomy (CCY) or colon polyp  
620 surgery) and free of other acute medical conditions were included and provided written informed  
621 consent preoperatively. Excess adipose tissue from the surgical site was collected at the  
622 discretion of the surgeon during the normal course of the procedure. The exclusion criteria were  
623 any subjects taking thiazolidinediones, chromatin-modifying enzymes such as valproic acid, anti-  
624 retroviral medications, and drugs known to induce insulin resistance such as mTOR inhibitors or  
625 systemic steroid medications. At UPMC, inclusion criteria were patients receiving bariatric  
626 surgery (Vertical Sleeve Gastrectomy or Roux en Y Gastric Bypass) or lean controls (hernia or  
627 CCY surgeries) ages 21-60, exclusion criteria were diagnosis of diabetes (Type 1 or Type 2),  
628 pregnancy, alcohol or drug addiction, bleeding or clotting abnormality, or inflammatory  
629 abdominal disease. All patients provided written informed consent preoperatively. Excess  
630 adipose tissue from the surgical site was collected at the discretion of the surgeon during the  
631 normal course of the procedure. 200-500 mg samples were flash frozen immediately after  
632 collection for downstream processing.

633

634 **Mouse adipose tissue samples**

635 All animal experiments were performed under a protocol approved by the BIDMC Institutional  
636 Animal Care and Use Committee. Male C57Bl/6J 16-week-old high fat diet fed (JAX 380050)  
637 and chow fed (JAX 380056) mice were obtained from The Jackson Laboratory and maintained  
638 on 60% high fat diet (Research Diets, D12492) or chow diet (8664 Harlan Teklad, 6.4% wt/wt  
639 fat), respectively, for three weeks before sacrifice. Female 6-week-old chow fed C57Bl/6J mice  
640 (JAX 380056) were maintained on 60% high fat diet for 13 weeks before sacrifice. Mice were  
641 maintained under a 12 hr light/12hr dark cycle at constant temperature (23°C) with free access to  
642 food and water.

643

#### 644 **Mature human adipocyte sample preparation**

645 *Purification of mature human adipocytes.*

646 Whole tissue subcutaneous adipose specimens were freshly collected from the operating room.  
647 Skin was removed, and adipose tissue was cut into 1- to 2-inch pieces and rinsed thoroughly with  
648 37°C PBS to remove blood. Cleaned adipose tissue pieces were quickly minced in an electric  
649 grinder with 3/16-inch hole plate, and 400 ml of sample was placed in a 2-l wide-mouthed  
650 Erlenmeyer culture flask with 100 ml of freshly prepared blendzyme (Roche Liberase TM,  
651 research grade, cat. no. 05401127001, in PBS, at a ratio of 6.25 mg per 50 ml) and shaken in a 37  
652 °C shaking incubator at 120 r.p.m. for 15–20 min to digest until the sample appeared uniform.  
653 Digestion was stopped with 100 ml of freshly made KRB (5.5 mM glucose, 137 mM NaCl, 15  
654 mM HEPES, 5 mM KCl, 1.25 mM CaCl<sub>2</sub>, 0.44 mM KH<sub>2</sub>PO<sub>4</sub>, 0.34 mM Na<sub>2</sub>HPO<sub>4</sub> and 0.8 mM  
655 MgSO<sub>4</sub>), supplemented with 2% BSA. Digested tissue was filtered through a 300 µM sieve and  
656 washed with KRB/albumin and flow through until only connective tissue remained. Samples  
657 were centrifuged at 233g for 5 min at room temperature, clear lipid was later removed, and

658 floated adipocyte supernatant was collected, divided into aliquots and flash-frozen in liquid  
659 nitrogen.

660

#### 661 *Sample selection and Bulk-RNA-seq library construction*

662 Fasting serum was collected and insulin, glucose, free fatty acids, and a lipid panel were  
663 measured by Labcorp. BMI measures were derived from electronic medical records and  
664 confirmed by self-reporting, and measures of insulin resistance, the homeostasis model  
665 assessment-estimated insulin resistance index (HOMA-IR) and revised quantitative insulin  
666 sensitivity check index (QUICKI) were calculated<sup>52,53</sup>. Female subjects in the first and fourth  
667 quartiles for either HOMA-IR or QUICKI and matched for age and BMI were processed for  
668 RNA-seq.

669

670 Total RNA from ~400  $\mu$ l of thawed floated adipocytes was isolated in TRIzol reagent  
671 (Invitrogen) according to the manufacturer's instructions. For RNA-seq library construction,  
672 mRNA was purified from 100 ng of total RNA by using a Ribo-Zero rRNA removal kit  
673 (Epicentre) to deplete ribosomal RNA and convert into double-stranded complementary DNA by  
674 using an NEBNext mRNA Second Strand Synthesis Module (E6111L). cDNA was subsequently  
675 tagged and amplified for 12 cycles by using a Nextera XT DNA Library Preparation Kit  
676 (Illumina FC-131). Sequencing libraries were analyzed with Qubit and Agilent Bioanalyzer,  
677 pooled at a final loading concentration of 1.8 pM and sequenced on a NextSeq500.

678

#### 679 **Single Cell and Single Nucleus sample preparation and processing**

680 *SVF isolation and Drop-seq.*

681 Adipose tissue samples were collected and processed as above. After removal of floated  
682 adipocytes, remaining supernatant was aspirated and the remaining pelleted stromal vascular  
683 fraction (SVF) was combined from multiple tubes. The combined SVF was washed 2 times with  
684 50ml cold PBS with 233g for 5 min centrifugation between washes. Erythrocytes were depleted  
685 with two rounds of 25 ml. ACK lysing buffer (Gibco™ A1049201) exposure (5 minutes at RT  
686 followed by 233g x 5 min centrifugation). Remaining SVF pellet was further washed x 2 with  
687 50ml cold PBS prior to counting on hematocytometer and loading onto Drop-seq microfluidic  
688 devices. Drop-seq was performed as described<sup>54</sup>, with the following modifications: first, flow  
689 rates of 2.1 mL/h were used for each aqueous suspension and 12 mL/h for the oil. Second,  
690 libraries were sequenced on the Illumina NextSeq500, using between 1.6-1.7 pM in a volume of  
691 1.2 mL HT1 and 3 mL of 0.3 μM Read1CustSeqB  
692 (GCCTGTCCGCGGAAGCAGTGGTATCAACGCAGAGTAC) using 20 x 8 x 60 read  
693 structure.

694

#### 695 *sNuc-Seq*

696 Nuclei were isolated from frozen mouse and human adipose tissue samples for 10x snRNA-seq  
697 using a slightly modified approach to what was previously described<sup>55-57</sup>. Samples were kept  
698 frozen on dry ice until immediately before nuclei isolation, and all sample handling steps were  
699 performed on ice. Each flash-frozen adipose tissue sample was placed into a gentleMACS C tube  
700 (Miltenyi Biotec) with 2 mL freshly prepared TST buffer (0.03% Tween 20 [Bio-Rad], 0.01%  
701 Molecular Grade BSA [New England Biolabs], 146 mM NaCl [ThermoFisher Scientific], 1 mM  
702 CaCl<sub>2</sub> [VWR International], 21 mM MgCl<sub>2</sub> [Sigma Aldrich], and 10 mM Tris-Hcl pH 7.5  
703 [ThermoFisher Scientific] in Ultrapure water [ThermoFisher Scientific]) with or without 0.2 U/

704  $\mu$ L of Protector RNase Inhibitor (Sigma Aldrich). gentleMACS C tubes were then placed on the  
705 gentleMACS Dissociator (Miltenyi Biotec) and tissue was dissociated by running the program  
706 “mr\_adipose\_01” twice, and then incubated on ice for 10 minutes. Lysate was passed through a  
707 40  $\mu$ m nylon filter (CellTreat) and collected into a 50 mL conical tube (Corning). Filter was  
708 rinsed with 3 mL of freshly prepared ST buffer buffer (146 mM NaCl, 1 mM CaCl<sub>2</sub>, 21 mM  
709 MgCl<sub>2</sub>; 10 mM Tris-Hcl pH 7.5) with or without 0.2 U/ $\mu$ L RNase Inhibitor, and collected into  
710 the same tube. Flow-through was centrifuged at 500 x g for 5 minutes at 4°C with brake set to  
711 low. Following centrifugation, supernatant was removed, and the nuclear pellet was resuspended  
712 in 50 - 200  $\mu$ l PBS pH 7.4 (ThermoFisher Scientific) with 0.02% BSA, with or without 0.2U/ $\mu$ L  
713 RNase Inhibitor. In order to reduce ambient mRNA, the nuclear pellets of some samples were  
714 washed 1-3 times with 5 mL of PBS-0.02% BSA before final resuspension. An aliquot of nuclei  
715 from each sample was stained with NucBlue (Thermofisher Scientific), counted in a  
716 hemocytometer using fluorescence to identify intact nuclei, and then immediately loaded on the  
717 10x Chromium controller (10x Genomics) according to the manufacturer’s protocol.  
718 For each sample, 10,000-16,500 nuclei were loaded in one channel of a Chromium Chip (10x  
719 Genomics). The Single Cell 3’ v3.1 chemistry was used to process all samples. cDNA and gene  
720 expression libraries were generated according to the manufacturer's instructions (10x Genomics).  
721 cDNA and gene expression library fragment sizes were assessed with a DNA High Sensitivity  
722 Bioanalyzer Chip (Agilent). cDNA and gene expression libraries were quantified using the Qubit  
723 dsDNA High Sensitivity assay kit (ThermoFisher Scientific). Gene expression libraries were  
724 multiplexed and sequenced on the Nextseq 500 (Illumina) with a 75-cycle kit and the following  
725 read structure: Read 1: 28 cycles, Read 2: 55 cycles, Index Read 1: 8 cycles.  
726

727 **Sequencing, read alignments, and quality control**

728 *Single-cell/nucleus RNA-seq data analysis.*

729 Raw sequencing reads were demultiplexed to FASTQ format files using bcl2fastq (Illumina;  
730 version 2.20.0). Digital expression matrices were generated from the FASTQ files using the  
731 Drop-Seq tools (<https://github.com/broadinstitute/Drop-seq>) pipeline, with appropriate  
732 adjustments made to the default program parameters to account for the different read-structures  
733 in the scRNA Drop-Seq data and sNuc 10X data. Reads from mouse and human were aligned  
734 with STAR<sup>58</sup> (version 2.7.3) against the GRCm38 and GRCh38 genome assemblies,  
735 respectively. Gene counts were obtained, per-droplet, by summarizing the unique read  
736 alignments across exons and introns in appropriate GENCODE annotations (release 16 of the  
737 mouse annotation and release 27 of the human annotation). In order to adjust for downstream  
738 effects of ambient RNA expression within mouse nuclei (hereafter “cells”), we used  
739 CellBender<sup>59</sup> (version 0.2.0) to remove counts due to ambient RNA molecules from the count  
740 matrices and to estimate the true cells. We also used CellBender to distinguish droplets  
741 containing cells from droplets containing only ambient RNA, by selecting droplets with >50%  
742 posterior probability of containing a cell. We compared the true cell estimation obtained using  
743 CellBender against the same using the DropletUtils software package<sup>60</sup>, which estimates ambient  
744 RNA expression levels but does not remove any ambient counts, keeping only the cells that were  
745 marked as not ambient by both algorithms. To address ambient RNA in the human sNuc data, we  
746 calculated spliced and unspliced RNA content in each cell, because nuclei have a high unspliced  
747 RNA content, a high percentage of spliced RNA indicates a high ambient RNA content. We  
748 therefore removed sNuc-seq cells containing over 75% spliced RNA. All samples were assessed  
749 for doublet content using scrublet<sup>61</sup> version 0.2.1, and cells called as doublets were removed



750 before further analysis. All cells were further filtered to have greater than 400 UMIs with <10%  
751 of UMIs from mitochondrial genes. Genes were filtered such that only genes detected in two or  
752 more cells were retained. For the human data, the median number of UMIs detected per cell was  
753 2559 and the median number of genes detected per cell was 1524. For the mouse data, the  
754 median number of UMIs detected per cell was 2291 and the median number of genes detected  
755 per cell was 1369.

756

#### 757 *Bulk RNA-seq Analysis.*

758 Raw sequencing reads were demultiplexed by using bcl2fastq (Illumina). Salmon<sup>62</sup> (version  
759 1.1.0) was used to simultaneously map and quantify transcript abundances of hg19 genes  
760 annotated by release 19 of the GENCODE project's human reference. Salmon was run using  
761 "full" selective alignment (SAF) with mapping validation as described previously<sup>63</sup>. Gene counts  
762 were summarized from transcript abundances using the "tximport" package for R<sup>64</sup>.

763

#### 764 **Integration, clustering, subclustering, and annotation**

765 Integration, clustering and subclustering analysis were performed using Seurat 3.9.9<sup>65</sup>. The gene  
766 counts were normalized using SCTransform<sup>66</sup>, and regressed on mitochondrial read percentage,  
767 ribosomal read percentage, and cell cycle score as determined by Seurat. In order to avoid  
768 smoothing over depot differences, for integration human and mouse data were grouped by  
769 'individual', i.e., if both subcutaneous and visceral adipose tissue for an individual human or  
770 mouse were available, they were pooled together during this step. Individuals were integrated  
771 with reciprocal PCA, using individuals that had both subcutaneous and visceral samples as  
772 references. As a result, the human and mouse references were comprised exclusively from the

773 sNuc seq cohort. To integrate, references were integrated together, then the remaining samples—  
774 sNuc seq individuals with only subcutaneous data as well as all Drop-seq samples—were  
775 mapped to the reference. For clustering, 5000 variable genes were used, and ribosomal and  
776 mitochondrial genes were removed from the variable gene set before running PCA and  
777 calculating clusters using a Louvain algorithm, 40 PCs, and a resolution of 0.5. Clusters were  
778 identified as adipocytes, preadipocytes, mesothelial cells, vascular cells, or immune cells using  
779 marker genes, subset into individual objects, and re-integrated using the above method. Samples  
780 with fewer than 50 cells in the subset were removed before re-integration. This led to samples  
781 having artificially fewer cells in some instances—for example some Drop-seq samples had cells  
782 that clustered with adipocytes, but these cells were removed in subclustering because the small  
783 numbers of cells introduced too much variability into the integration. Subclustering was  
784 performed using a range of variable genes (1000-2000), PCs (10-40) and resolutions (0.2-0.6).  
785 Markers were calculated using a non-parametric Wilcoxon rank sum test and clusters were  
786 evaluated based on the distinctness of called markers to determine the final subclustering  
787 conditions. In the subclustered objects, we removed clusters that appeared to represent doublets  
788 based on the score assigned by scrublet<sup>61</sup>, or that appeared to be driven by high ambient RNA  
789 content as determined by levels of mitochondrial genes and spliced/unspliced RNA ratio. The  
790 remaining clusters were annotated based on marker gene expression. In some cases, smaller  
791 subclusters (T and NK cells, B cells, monocytes/neutrophils) were further subset and PCA and  
792 clustering analysis but not integration was re-run in order to assign clusters. After subcluster  
793 annotation, identities were mapped back onto the original object and cells that were removed  
794 from the subclustered objects were similarly removed from the all-cell object.  
795

## 796 **Deconvolution of bulk RNA-seq data**

797 Bulk RNA sequencing data for subcutaneous adipose tissue from the METSIM cohort were  
798 obtained as described previously<sup>13</sup>. Only individuals with available metabolic phenotyping data  
799 were used for the deconvolution analysis. Bulk RNA sequencing data for floated human  
800 adipocytes were obtained described above. Deconvolution analysis was performed using  
801 MuSiC<sup>12</sup> (version 0.1.1) with human sNuc subcutaneous all cell or adipocyte data as reference.  
802 Marker genes used for deconvolution can be found in **Supplemental Table 1**.

803

## 804 **Comparison between mouse and human datasets**

805 Mapping of mouse cells onto human clusters was performed using Seurat multimodal reference  
806 mapping<sup>67</sup>. To run, for the all-cell and each subset, the mouse data was prepared by extracting  
807 the counts matrix from the mouse sNuc object and mapping the mouse gene names to their  
808 human orthologs using a database of ortholog mappings from Mouse Genome Informatics  
809 (<http://www.informatics.jax.org/homology.shtml>). In the case of multi-mapping, the first  
810 ortholog pair was used. The mouse object was then split by sample and mapped onto the sNuc-  
811 seq data from the matching human all-cell or subset object using the RNA assay and PCA  
812 reduction.

813

## 814 **Immunohistochemistry**

815 Subcutaneous (abdominal) and omental adipose tissue biopsies belonging to lean and obese  
816 women (GRIA4: subcutaneous, 5 lean and 5 obese individuals; PGAP1: subcutaneous, 5 lean, 4  
817 obese, visceral 3 lean, 4 obese; EBF2: omental, 3 lean and 4 obese individuals; AGMO:  
818 subcutaneous, 4 lean and 4 obese individuals, for all experiments two slides per individual for

819 GRIA4, EBF2, AGMO, one slide per individual for PGAP1) were fixed (overnight in 4%  
820 paraformaldehyde at 4°C, dehydrated, paraffin embedded and sectioned (4µm thick). The  
821 following primary antibodies and respective dilution were used: GRIA4, 1:200, Cat #23350-1-AP,  
822 Proteintech; PGAP1, 1:400, Cat. #55392-1-AP, Proteintech EBF2, 1:1000, Cat. #AF7006, R&D  
823 systems; AGMO (TMEM195) 1:100, Cat #orb395684, Biorbyt. In brief, after rinsing in PBS,  
824 tissue slices were blocked with 3% normal goat serum and incubated with the primary antibody in  
825 PBS, overnight at 4°C. After a thorough rinse in PBS, sections were incubated in 1:200 v/v  
826 biotinylated secondary antibody solution for 30 minutes (Invitrogen), rinsed in PBS and incubated  
827 in avidin-biotin-peroxidase complex (ABC Standard, Vector Laboratories), washed several times  
828 in PBS and lastly incubated in 3,3'-diaminobenzidine tetrahydrochloride (0.05% in 0.05 M Tris  
829 with 0.03% H<sub>2</sub>O<sub>2</sub>; 5 min). After immunohistochemical staining, sections were counterstained with  
830 hematoxylin, dehydrated in ethanol, cleared in xylene and covered with coverslip using Eukitt  
831 (Merck). All observations were performed using Nikon Eclipse E800 light microscope.

832

### 833 **Immunofluorescence microscopy of mature human adipocytes**

834 Adipocyte immunofluorescence protocol was adapted from Sárvári et al<sup>9</sup>. Abdominal  
835 subcutaneous adipose tissue was collected from two adult female human subjects (BMI 24.9 and  
836 40.3) as above and placed on ice. Tissue was minced and digested with 1 mg/mL type II  
837 collagenase (Sigma-Aldrich, C6885) in Hanks' balanced salt solution supplemented with 0.5%  
838 fatty acid-free BSA (Sigma-Aldrich, A6003) at 37° in a water bath with constant shaking at 250  
839 rpm. The cell suspension was filtered through a 250 µM nylon mesh strainer (Thermo, 87791)  
840 and washed three times with Krebs-Ringer bicarbonate buffer containing 1% fatty acid-free  
841 BSA. All washes throughout this protocol were performed without centrifugation to minimize

842 adipocyte damage and loss; cell suspension was maintained upright for at least 5 minutes to  
843 allow mature adipocytes to float, and infranatant was removed with a needle and syringe. The  
844 floating adipocytes were fixed with 2% PFA and 1% sucrose in PBS for 30 minutes with  
845 constant rotation followed by three washes with 2% fatty acid-free BSA in PBS. Adipocytes  
846 were subsequently permeabilized with 0.5% Triton-X (Thermo, 28314) in PBS for five minutes,  
847 and incubated with 2.5 µg/mL trypsin (Corning, 25053CI) in PBS for 10 minutes at 37° in a  
848 water bath with constant shaking. Adipocytes were then blocked with 2% fatty acid-free BSA in  
849 PBS for 30 minutes, and incubated overnight at room temperature with rabbit polyclonal anti-  
850 GRIA4 (Proteintech, 23350-1-AP) diluted 1:100 in 500 µL 2% fatty acid-free BSA in PBS with  
851 constant rotation. The adipocytes were then washed twice for 10 minutes each with 0.1% fatty  
852 acid-free BSA and 0.05% Tween-20 (Sigma-Aldrich, P9416) in PBS, followed by incubation  
853 with goat anti-rabbit Alexa Fluor 546 (Thermo, A-11035) secondary antibody diluted 1:500 in  
854 2% fatty acid-free BSA for 2 hours with rotation. For the final 30 minutes of incubation, Hoechst  
855 33342 (Thermo, 62249) and BODIPY 493/503 (Invitrogen, D3922) were added at 1:500  
856 dilutions. Adipocytes were washed twice and resuspended in 300 µL Fluoromount G (Southern  
857 Biotech, 0100-01) and mounted on glass slides with 1.4-1.6 mm concavity wells (Electron  
858 Microscopy Sciences, 71878-03). A sample of adipocytes was also incubated as above but  
859 without primary antibody to verify the specificity of the secondary antibody. Fluorescence  
860 images were acquired using Zeiss LSM 880 Upright Laser Scanning Confocal Microscope with  
861 filter cubes for DAPI, GFP, and Rhodamine in parallel using the 20X objective and processed  
862 using Zen Black 2.3 software. Images were analyzed and counted with ImageJ v. 1.53k.  
863

864 ***Ex vivo* differentiation and transcriptional and high-content image-based characterization**  
865 **of differentiating primary human adipocyte progenitors**

866 We obtained adipocyte progenitors from subcutaneous and visceral adipose tissue from patients  
867 undergoing a range of abdominal laparoscopic surgeries (sleeve gastrectomy, fundoplication or  
868 appendectomy). The visceral adipose tissue is derived from the proximity of the angle of His and  
869 subcutaneous adipose tissue obtained from beneath the skin at the site of surgical incision.

870 Additionally, human liposuction material was obtained. Each participant gave written informed  
871 consent before inclusion and the study protocol was approved by the ethics committee of the  
872 Technical University of Munich (Study № 5716/13). Isolation of AMSCs was performed as  
873 previously described<sup>28</sup>, and cells were differentiated in culture over 14 days. *Ex vivo*

874 differentiated adipocytes were stained and imaged, and features were extracted using

875 LipocyteProfiler as described in Laber et al. RNA-sequencing libraries were prepared and  
876 sequenced and QC'ed as previously described<sup>28</sup>. Bulk-RNA sequencing counts from

877 subcutaneous and visceral samples differentiated for 14 days were deconvoluted using both

878 subcutaneous and visceral adipocytes as reference as described above. Raw images collected

879 during LipocyteProfiler analysis were randomly selected from samples predicted to have high or

880 low content of hAd3, hAd5, or hAd6 adipocytes, and pseudocolored and combined using Adobe

881 Photoshop.

882

883 **Gene Pathway Analysis**

884 Analysis of enriched pathways in adipocyte markers was performed using clusterProfiler<sup>68</sup>

885 (version 3.16.1). Adipocyte cluster markers were filtered to an adjusted *p*-value < .05, then

886 evaluated for enrichment in GO biological pathways or KEGG pathways containing under 300  
887 genes.

888

### 889 **Identification and analysis of EBF2 SNP association with visceral adiposity**

890 VAT, ASAT, and GFAT volumes in 40,032 individuals from the UK Biobank<sup>69,70</sup> who  
891 underwent MRI imaging were quantified as described elsewhere<sup>71</sup>. Variant rs4872393 was  
892 identified as a lead SNP associated with VATadjBMI and waist-to-hip ratio from summary  
893 statistics of two prior studies<sup>31,72</sup>. Among the cohort who underwent MRI imaging, all variants at  
894 this locus ( $\pm$  250 kb around rs4872393) with MAF  $\geq$  0.005 and imputation quality (INFO)  
895 score  $\geq$  0.3 were analyzed. For all 554 nominally significant ( $P < 0.05$ ) variants associated with  
896 VATadjBMI in this region, a secondary conditional analysis testing for association with  
897 VATadjBMI was performed controlling for rs4872393 carrier status ( $P < 0.05/554 = 9 \times 10^{-5}$ ).  
898 Participants were excluded from analysis if they met any of the following criteria: (1) mismatch  
899 between self-reported sex and sex chromosome count, (2) sex chromosome aneuploidy, (3)  
900 genotyping call rate  $< 0.95$ , or (4) were outliers for heterozygosity. Up to 37,641 participants  
901 were available for analysis. Fat depot volumes adjusted for BMI and height (“adj” traits) were  
902 calculated by taking the residuals of the fat depot in sex-specific linear regressions against age at  
903 the time of MRI, age squared, BMI, and height<sup>31</sup>. Each trait was scaled to mean 0 and variance 1  
904 in sex-specific groups before being combined for analysis. Linear regressions between a given  
905 trait-variant pair were adjusted for age at the time of imaging, age squared, sex, the first 10  
906 principal components of genetic ancestry, genotyping array, and MRI imaging center. Analyses  
907 were performed using R 3.6.0 (R Project for Statistical Computing). *EBF2* regional visualization  
908 plot was made with the LocusZoom online tool<sup>73</sup>.

909

## 910 **Calculation of pseudobulk datasets to estimate adipose innervation**

911 Approximate bulk RNA-seq datasets (pseudobulk) were obtained for visceral sNuc-seq samples  
912 by summing the total expression per-gene across all droplets containing a valid 10X cell barcode.  
913 This includes all cells that would normally have been removed in the single-nuclei studies by any  
914 of the filtering criteria (above): doublet score, splicing content, droplets with fewer than 400  
915 UMIs, etc, in order to preserve the ambient RNA present in otherwise empty droplets. Repeated  
916 UMIs were still collapsed into single counts (per-droplet) before summing. Levels of pan-  
917 neuronal markers were calculated using this pseudobulk dataset and plotted against the  
918 proportion of visceral populations hAd2 and hAd6 relative to total adipocytes in each sample.

919

## 920 **Prediction of cell-cell interactions**

921 Analysis of cell-cell interactions was performed using CellphoneDB<sup>41</sup> (version 2.0.0). For human  
922 data, sNuc-seq counts data was split into files containing cells from subcutaneous and visceral fat  
923 from individuals with BMI lower than 30 or higher than 40. CellphoneDB with statistical  
924 analysis was run on each file separately to evaluate interactions in each condition. For mouse  
925 data, counts data was split into files containing cells from the inguinal and perigonadal fat of  
926 chow and high fat diet fed mice. Mouse gene names were converted to human gene names, as  
927 above, before running CellphoneDB with statistical analysis on each file.

928

## 929 **Identification of candidate etiologic cell types using CELLEX and CELLECT**

930 CELLECT (<https://github.com/perslab/CELLECT>) and CELLEX

931 (<https://github.com/perslab/CELLEX>) were used to identify candidate etiological cell types for a



932 total of 23 traits. The input data for CELLECT is GWAS summary statistics for a given trait and  
933 cell type expression specificity (ES) estimates derived from single-cell RNA-seq data. The  
934 output is a list of prioritized candidate etiologic cell types for a given trait. ES estimates were  
935 calculated using CELLEX (version 1.1), which computes robust estimates of ES by relying on  
936 multiple expression specificity measures (for further details see Timshel et. al.<sup>74</sup>). CELLEX was  
937 run separately on the raw mouse and human (sNuc) gene expression matrices to compute gene  
938 expression specificities for each cluster based on the clustering assignment reported above. The  
939 resulting cell type specificity matrix was used along with multiple GWAS studies<sup>30,75–79</sup>  
940 (**Extended Data Table 3**) as input for CELLECT<sup>74</sup> (version 1.1), which was run with default  
941 parameters. Significant cell types were identified using a by-trait and by-species Bonferroni *p*-  
942 value threshold of  $p < 0.05$ .

943

#### 944 **SNP analysis for bulk mRNA-seq cohort**

945 The raw GTC SNP expression data from Infinium OmniExpress-24 Kit was converted to VCF  
946 format using Picard version 2.21.6. The pre-processing of the SNP data before phasing and  
947 imputation was performed using plink2 (<https://www.cog-genomics.org/plink/2.0/>). The SNP  
948 genotype was then phased and imputed using the Eagle v2.3.5<sup>80</sup> and Minimac3<sup>81</sup> packages,  
949 respectively. SNPs were mapped to the NCBI database using the rsnp package  
950 (<https://CRAN.R-project.org/package=rsnps>) and filtered to keep only SNPs that had a minor  
951 allele frequency  $> 0.05$ . For plotting gene expression against genotype, bulk RNA sequencing  
952 data was TMM normalized using edgeR<sup>82</sup>. Statistical validation for significance was done using  
953 the Wilcoxon rank-sum Test which is a non-parametric test assuming independent samples.

954

955 **Statistics**

956 *p*-values for scatterplots were calculated using GraphPad Prism version 8.0 and represent the  
957 probability that the slope of the line of best fit is nonzero. All error bars on bar graphs represent  
958 standard error. Statistics on proportional composition graphs were calculated using scCODA<sup>83</sup>  
959 (version 0.1.2) using the Hamiltonian Monte Carlo sampling method. The model formula used  
960 was “Depot + BMI” (human) or “Depot + Diet” (mouse) for all objects in for which both of these  
961 covariates were present, or the individual covariate when only a single condition was present.

962

963 **DATA AVAILABILITY**

964 Single cell RNA expression and count data is deposited in the Single Cell Portal (Study  
965 [#SCP1376](#)) and will be downloadable upon publication. Processed count data for bulk RNA-seq  
966 and dge matrices for single cell and single nucleus RNA-seq have been deposited in GEO and  
967 will be made public upon publication (Bulk-seq Accession #GSE174475, sc-RNA-seq/sNuc-seq  
968 Accession #GSE176171), raw sequencing reads for mouse data will additionally be deposited  
969 before publication. FASTQ and SNP array files for human samples will be deposited in dbGaP  
970 before publication.

971

972 **CODE AVAILABILITY**

973 Data analysis pipelines used in this study for processing of raw sequencing data, integration, and  
974 clustering can be obtained from <https://gitlab.com/rosen-lab/white-adipose-atlas>.

975 **METHODS REFERENCES**

- 976 52. Katz, A. *et al.* Quantitative Insulin Sensitivity Check Index: A Simple, Accurate Method  
977 for Assessing Insulin Sensitivity In Humans. *J. Clin. Endocrinol. Metab.* **85**, 2402–2410  
978 (2000).
- 979 53. Matthews, D. R. *et al.* Homeostasis model assessment: insulin resistance and  $\beta$ -cell  
980 function from fasting plasma glucose and insulin concentrations in man. *Diabetologia* **28**,  
981 412–419 (1985).
- 982 54. Macosko, E. Z. *et al.* Highly Parallel Genome-wide Expression Profiling of Individual  
983 Cells Using Nanoliter Droplets. *Cell* **161**, 1202–1214 (2015).
- 984 55. Drokhlyansky, E. *et al.* The Human and Mouse Enteric Nervous System at Single-Cell  
985 Resolution. *Cell* **182**, 1606-1622.e23 (2020).
- 986 56. Slyper, M. *et al.* A single-cell and single-nucleus RNA-Seq toolbox for fresh and frozen  
987 human tumors. *Nat. Med.* **26**, 792–802 (2020).
- 988 57. Delorey, T. M. *et al.* A single-cell and spatial atlas of autopsy tissues reveals pathology  
989 and cellular targets of SARS-CoV-2. *bioRxiv* (2021) doi:10.1101/2021.02.25.430130.
- 990 58. Dobin, A. *et al.* STAR: ultrafast universal RNA-seq aligner. *Bioinforma. Oxf. Engl.* **29**,  
991 15–21 (2013).
- 992 59. CellBender remove-background: a deep generative model for unsupervised removal of  
993 background noise from scRNA-seq datasets | bioRxiv.  
994 <https://www.biorxiv.org/content/10.1101/791699v1>.
- 995 60. Lun, A. T. L. *et al.* EmptyDrops: distinguishing cells from empty droplets in droplet-  
996 based single-cell RNA sequencing data. *Genome Biol.* **20**, 63 (2019).

- 997 61. Wolock, S. L., Lopez, R. & Klein, A. M. Scrublet: Computational Identification of Cell  
998 Doublets in Single-Cell Transcriptomic Data. *Cell Syst.* **8**, 281-291.e9 (2019).
- 999 62. Patro, R., Duggal, G., Love, M. I., Irizarry, R. A. & Kingsford, C. Salmon provides fast  
1000 and bias-aware quantification of transcript expression. *Nat. Methods* **14**, 417–419 (2017).
- 1001 63. Srivastava, A. *et al.* Alignment and mapping methodology influence transcript abundance  
1002 estimation. *Genome Biol.* **21**, 239 (2020).
- 1003 64. Sonesson, C., Love, M. I. & Robinson, M. D. Differential analyses for RNA-seq:  
1004 transcript-level estimates improve gene-level inferences. *F1000Research* **4**, 1521 (2015).
- 1005 65. Stuart, T. *et al.* Comprehensive integration of single-cell data. *Cell* **177**, 1888-1902.e21  
1006 (2019).
- 1007 66. Hafemeister, C. & Satija, R. Normalization and variance stabilization of single-cell RNA-  
1008 seq data using regularized negative binomial regression. *Genome Biol.* **20**, 296 (2019).
- 1009 67. Hao, Y. *et al.* Integrated analysis of multimodal single-cell data. *bioRxiv*  
1010 2020.10.12.335331 (2020) doi:10.1101/2020.10.12.335331.
- 1011 68. Yu, G., Wang, L.-G., Han, Y. & He, Q.-Y. clusterProfiler: an R Package for Comparing  
1012 Biological Themes Among Gene Clusters. *OMICS J. Integr. Biol.* **16**, 284–287 (2012).
- 1013 69. Littlejohns, T. J. *et al.* The UK Biobank imaging enhancement of 100,000 participants:  
1014 rationale, data collection, management and future directions. *Nat. Commun.* **11**, 2624 (2020).
- 1015 70. Sudlow, C. *et al.* UK Biobank: An Open Access Resource for Identifying the Causes of a  
1016 Wide Range of Complex Diseases of Middle and Old Age. *PLOS Med.* **12**, e1001779 (2015).
- 1017 71. Agrawal, S. *et al.* Association of machine learning-derived measures of body fat  
1018 distribution in >40,000 individuals with cardiometabolic diseases. 2021.05.07.21256854

- 1019 <https://www.medrxiv.org/content/10.1101/2021.05.07.21256854v1> (2021)
- 1020 doi:10.1101/2021.05.07.21256854.
- 1021 72. Kichaev, G. *et al.* Leveraging Polygenic Functional Enrichment to Improve GWAS  
1022 Power. *Am. J. Hum. Genet.* **104**, 65–75 (2019).
- 1023 73. Pruim, R. J. *et al.* LocusZoom: regional visualization of genome-wide association scan  
1024 results. *Bioinforma. Oxf. Engl.* **26**, 2336–2337 (2010).
- 1025 74. Timshel, P. N., Thompson, J. J. & Pers, T. H. Genetic mapping of etiologic brain cell  
1026 types for obesity. *eLife* **9**, e55851 (2020).
- 1027 75. Mahajan, A. *et al.* Fine-mapping type 2 diabetes loci to single-variant resolution using  
1028 high-density imputation and islet-specific epigenome maps. *Nat. Genet.* **50**, 1505–1513  
1029 (2018).
- 1030 76. Loh, P.-R., Kichaev, G., Gazal, S., Schoech, A. P. & Price, A. L. Mixed-model  
1031 association for biobank-scale datasets. *Nat. Genet.* **50**, 906–908 (2018).
- 1032 77. Finucane, H. K. *et al.* Partitioning heritability by functional annotation using genome-  
1033 wide association summary statistics. *Nat. Genet.* **47**, 1228–1235 (2015).
- 1034 78. Teslovich, T. M. *et al.* Biological, clinical and population relevance of 95 loci for blood  
1035 lipids. *Nature* **466**, 707–713 (2010).
- 1036 79. Bradfield, J. P. *et al.* A Genome-Wide Meta-Analysis of Six Type 1 Diabetes Cohorts  
1037 Identifies Multiple Associated Loci. *PLOS Genet.* **7**, e1002293 (2011).
- 1038 80. Loh, P.-R. *et al.* Reference-based phasing using the Haplotype Reference Consortium  
1039 panel. *Nat. Genet.* **48**, 1443–1448 (2016).
- 1040 81. Das, S. *et al.* Next-generation genotype imputation service and methods. *Nat. Genet.* **48**,  
1041 1284–1287 (2016).

- 1042 82. Robinson, M. D., McCarthy, D. J. & Smyth, G. K. edgeR: a Bioconductor package for  
1043 differential expression analysis of digital gene expression data. *Bioinformatics* **26**, 139–140  
1044 (2010).
- 1045 83. Büttner, M., Ostner, J., Müller, C., Theis, F. & Schubert, B. scCODA: A Bayesian model  
1046 for compositional single-cell data analysis. *bioRxiv* 2020.12.14.422688 (2020)  
1047 doi:10.1101/2020.12.14.422688.
- 1048 84. Cawthorn, W. P., Scheller, E. L. & MacDougald, O. A. Adipose tissue stem cells meet  
1049 preadipocyte commitment: going back to the future[S]. *J. Lipid Res.* **53**, 227–246 (2012).
- 1050 85. Ferrero, R., Rainer, P. & Deplancke, B. Toward a Consensus View of Mammalian  
1051 Adipocyte Stem and Progenitor Cell Heterogeneity. *Trends Cell Biol.* **30**, 937 (2020).

1052

#### 1053 ACKNOWLEDGEMENTS

1054 This work was supported by NIH grants RC2 DK116691 to EDR, LTT, AC, OA, and AR, AHA  
1055 POST14540015 and DoD PRMRP-DAW81XWH to LTT, Broad-BADERC Collaboration  
1056 Initiative Award (NIH 5P30DK057521) to LTT and EDR, and R01 DK102173 to EDR. MPE is  
1057 supported by NIH grant F32DK124914. Additional support includes PRIN 2017 (Italian Ministry  
1058 of University, #2017L8Z2EM) to AG, THP acknowledges the Novo Nordisk Foundation  
1059 (unconditional donation to the Novo Nordisk Foundation Center for Basic Metabolic Research;  
1060 grant number NNF18CC0034900) and the Lundbeck Foundation (Grant number R190-2014-  
1061 3904), grants AMP-T2D RFB8b (FNIH) and UM1DK126185 (NIDDK) to MC, Sarnoff  
1062 Cardiovascular Research Foundation Fellowship to S.A., grants 1K08HG010155 and  
1063 1U01HG011719 to A.V.K. from the National Human Genome Research Institute, and a  
1064 sponsored research agreement from IBM Research to the Broad Institute of MIT and Harvard to

1065 A.V.K. All single cell library construction and sequencing was performed through the Boston  
1066 Nutrition Obesity Research Center Functional Genomics and Bioinformatics Core (NIH  
1067 P30DK046200). We thank Christina Usher for artistic support and Miriam Udler for helpful  
1068 discussions.

1069

#### 1070 AUTHOR CONTRIBUTIONS

1071 MPE, LTT, and EDR conceived of the project. MPE and EDR wrote the manuscript with  
1072 assistance from LTT, CJ, OA, and AR. MPE, ALE, DP, DT, GC, ADV, AS, EM, SS, SL, GPW,  
1073 MLV, and AGu performed experiments. GPW, AGu, ZK, JD, CGB, WG, AC, SJL, BTL, DM,  
1074 and AT collected samples. MPE, CJ, AMJ, HD, SA, AK, and HS performed computational  
1075 analysis. AVK, MC, THP, AGi, OA, and AR provided additional intellectual input.

1076

#### 1077 COMPETING INTEREST DECLARATION

1078 S.A. has served as a scientific consultant to Third Rock Ventures. A.V.K. has served as a  
1079 scientific advisor to Sanofi, Amgen, Maze Therapeutics, Navitor Pharmaceuticals, Sarepta  
1080 Therapeutics, Novartis, Verve Therapeutics, Silence Therapeutics, Veritas International, Color  
1081 Health, Third Rock Ventures, and Columbia University (NIH); received speaking fees from  
1082 Illumina, MedGenome, Amgen, and the Novartis Institute for Biomedical Research; and received  
1083 a sponsored research agreement from the Novartis Institute for Biomedical Research. M.C. holds  
1084 equity in Waypoint Bio and is a member of the Nestle Scientific Advisory Board. A.R. is a co-  
1085 founder and equity holder of Celsius Therapeutics, an equity holder in Immunitas Therapeutics  
1086 and a scientific advisory board member of Thermo Fisher Scientific, Syros Pharmaceuticals,

1087 Asimov and Neogene Therapeutics. A.R. is also an employee of Genentech. All other authors

1088 declare no competing interests.

1089

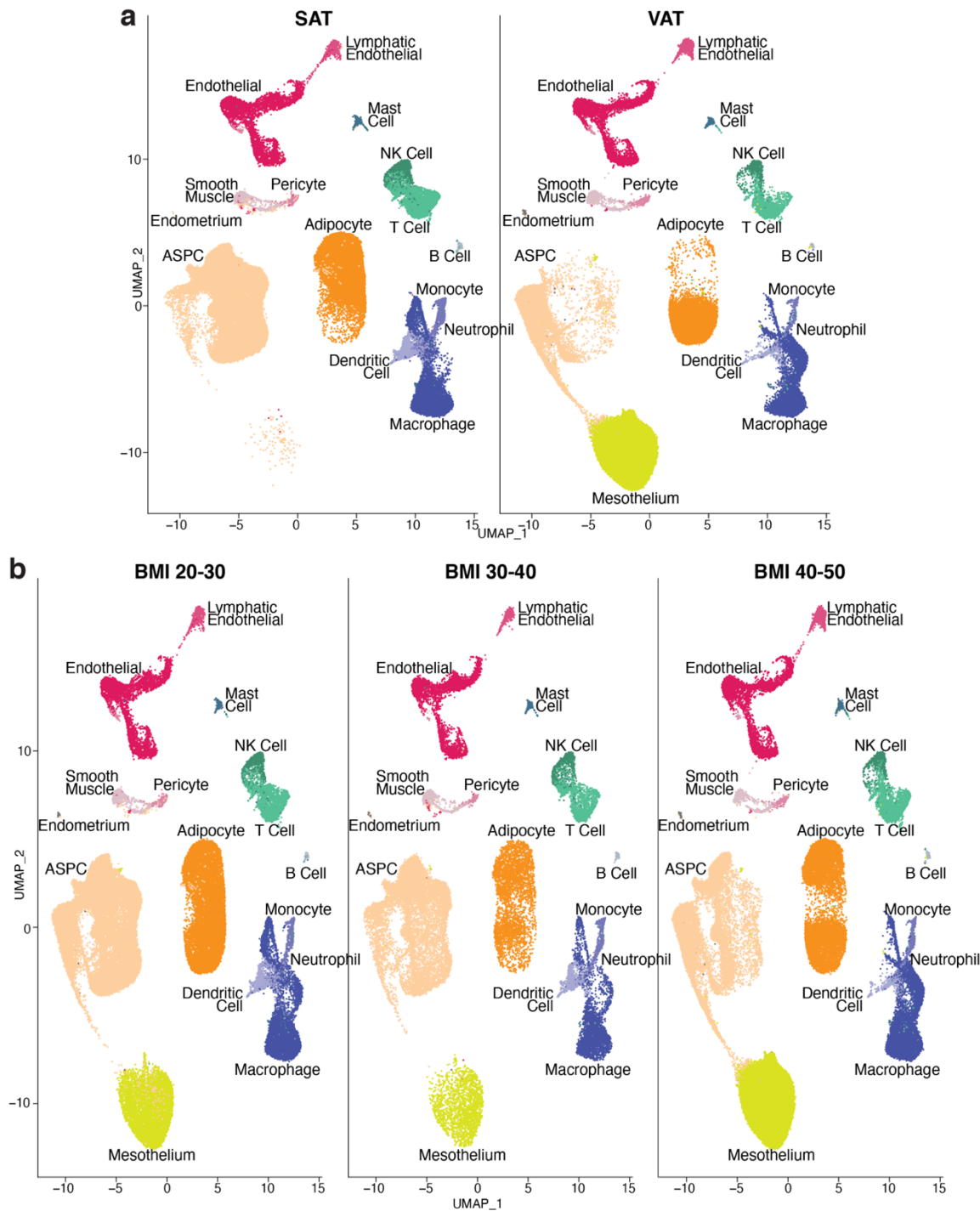
1090 ADDITIONAL INFORMATION

1091 Supplementary information is available for this paper.

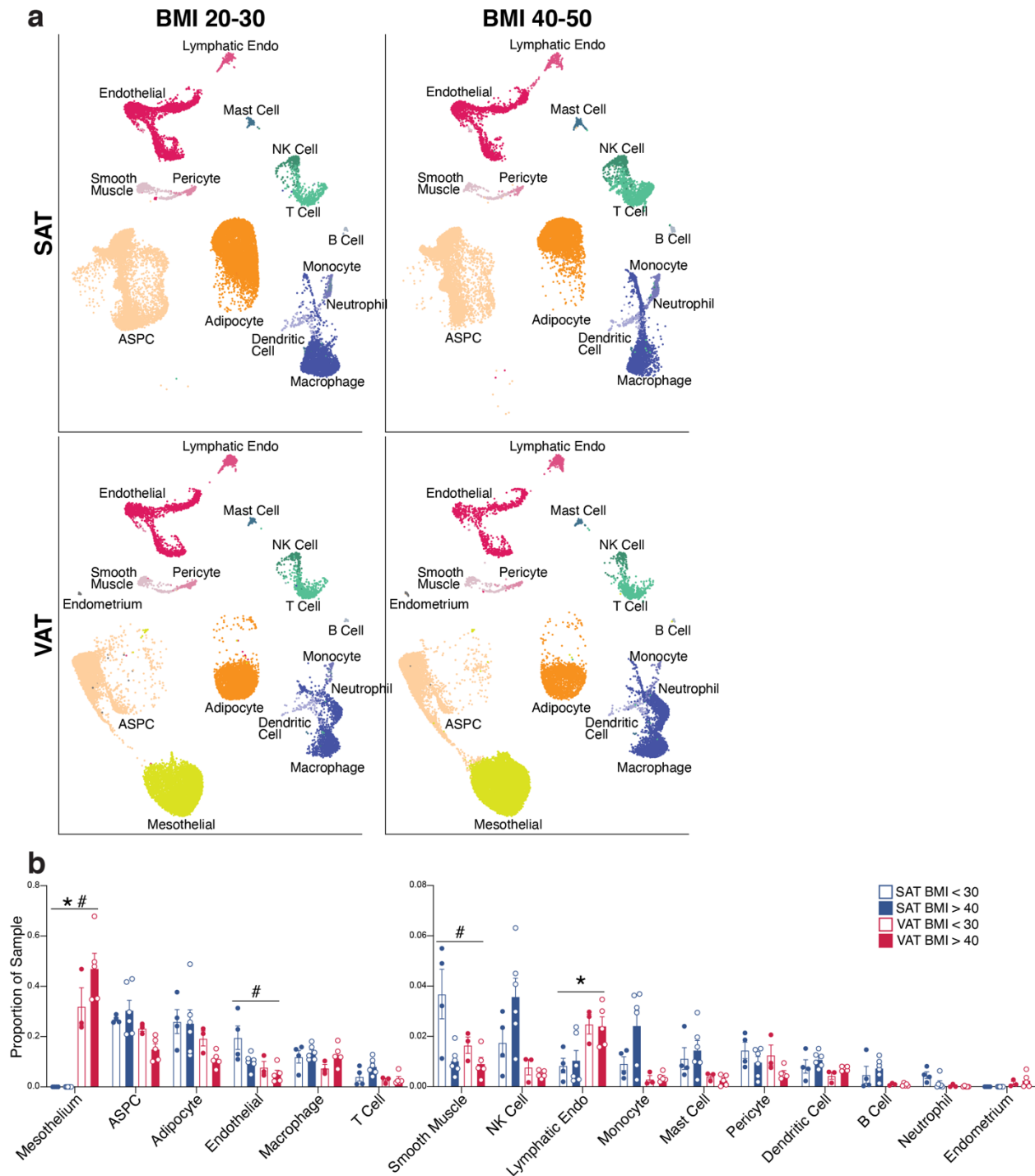
1092 Correspondence and requests for materials should be addressed to EDR.



1093 **EXTENDED DATA FIGURE AND TABLE LEGENDS**



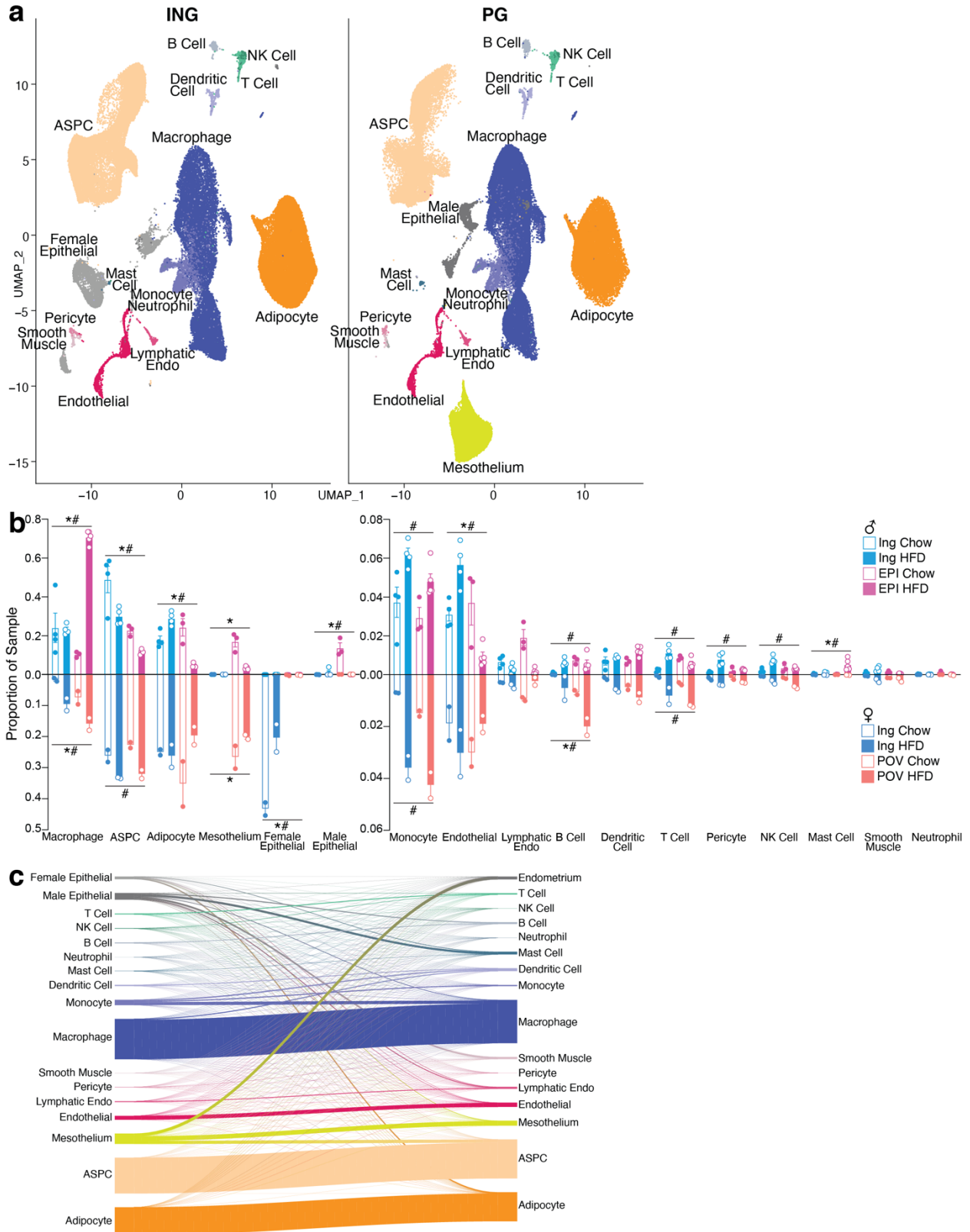
1094 **Extended Data Fig. 1. Recovery of human WAT cell types is highly influenced by adipose**  
1095 **depot. a, UMAP projection of all human cells split by depot. b, UMAP projection of all human**  
1096 **cells split by BMI range.**



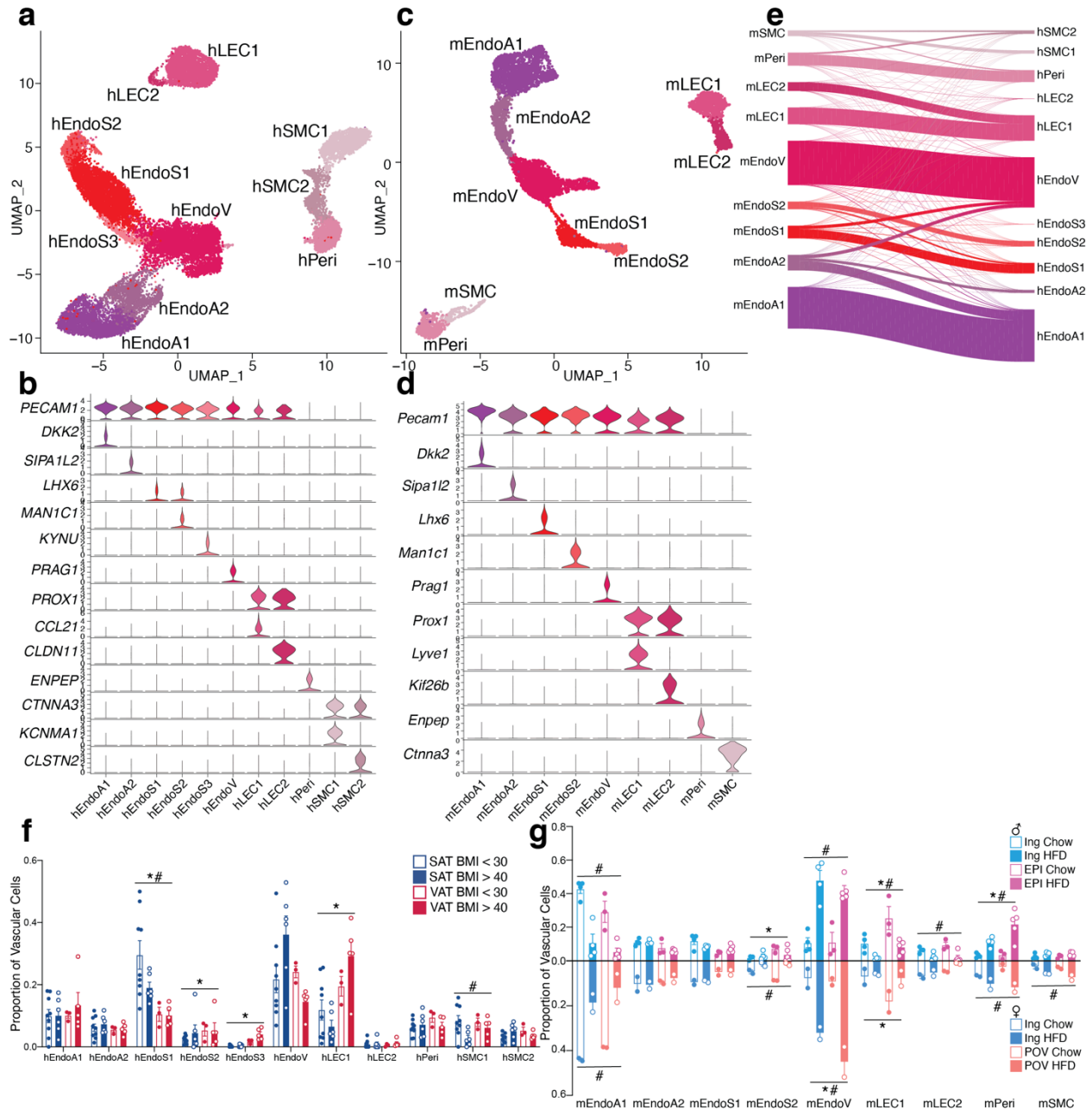
1097 **Extended Data Fig. 2. Additional analysis of the effects of depot and BMI on human WAT**

1098 **populations. a, UMAP projections of cells from the lowest and highest BMI ranges in the**

1099 dataset, split by depot. To facilitate comparison, samples were randomly subset to contain the  
1100 same number of cells in each plot ( $n = 20,339$ ). **b**, Graph showing the proportion of sNuc-seq  
1101 cells in each cluster per sample, split by depot and BMI. For bar graphs, \* indicates credible  
1102 depot effect and # indicates credible BMI effect, calculated using dendritic cells as reference.

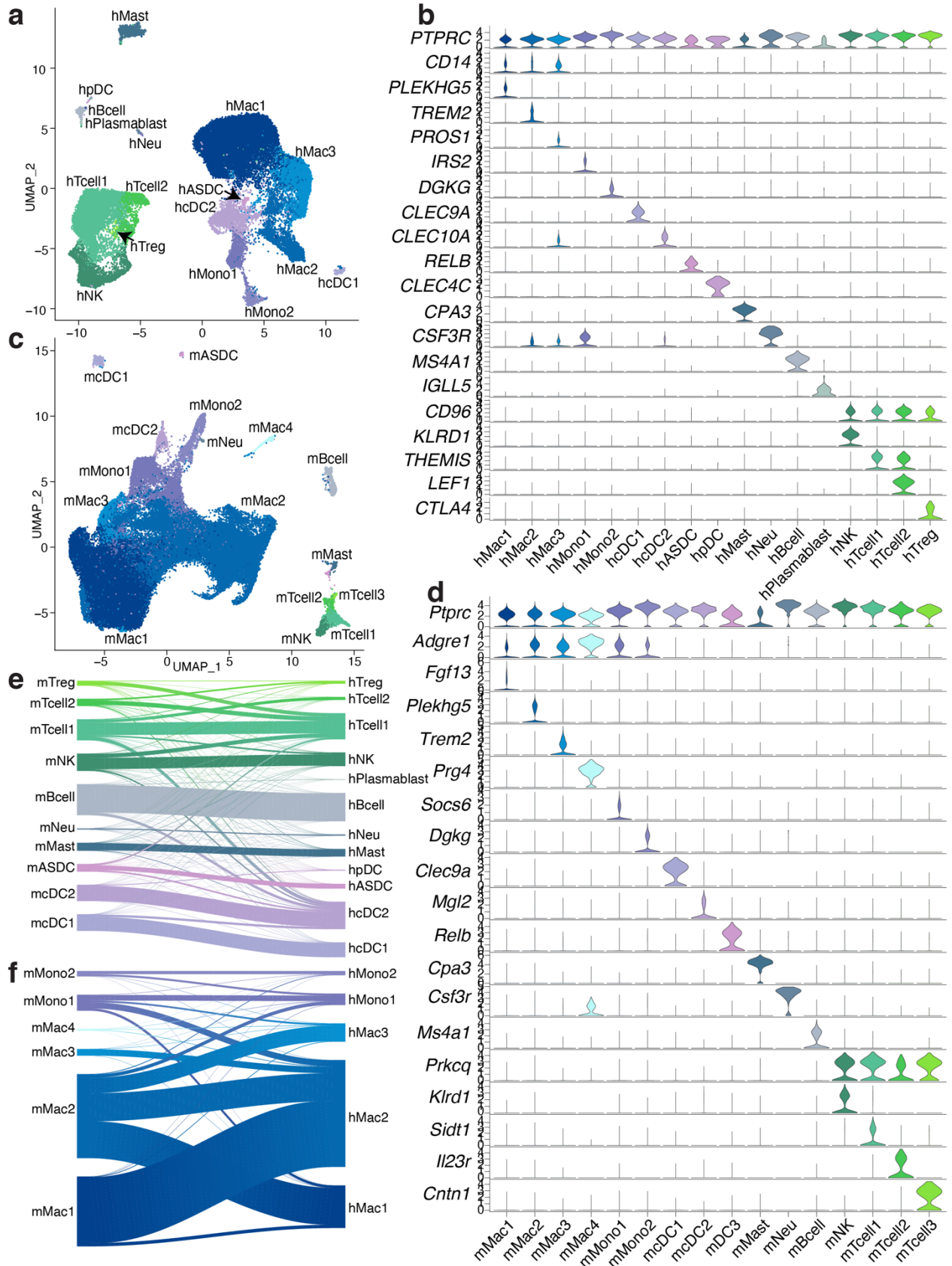


1103 **Extended Data Fig. 3. Additional analysis of the effects of depot and diet on mouse WAT**  
1104 **populations and association with human WAT populations. a**, UMAP projection of all mouse  
1105 WAT cells split by depot. **b**, Proportion of cells in each cluster per sample, split by sex as well as  
1106 by depot and diet. **c**, Riverplot showing the relationship between mouse and human clusters.  
1107 Mouse cells were mapped onto human sNuc-seq cells using multimodal reference mapping. The  
1108 riverplot represents the relationship between manually assigned mouse cluster and mapped  
1109 human cluster for every mouse cell. For bar graph, error bars represent SEM, \* indicates credible  
1110 depot effect and # indicates credible diet effect, calculated using dendritic cells as reference.



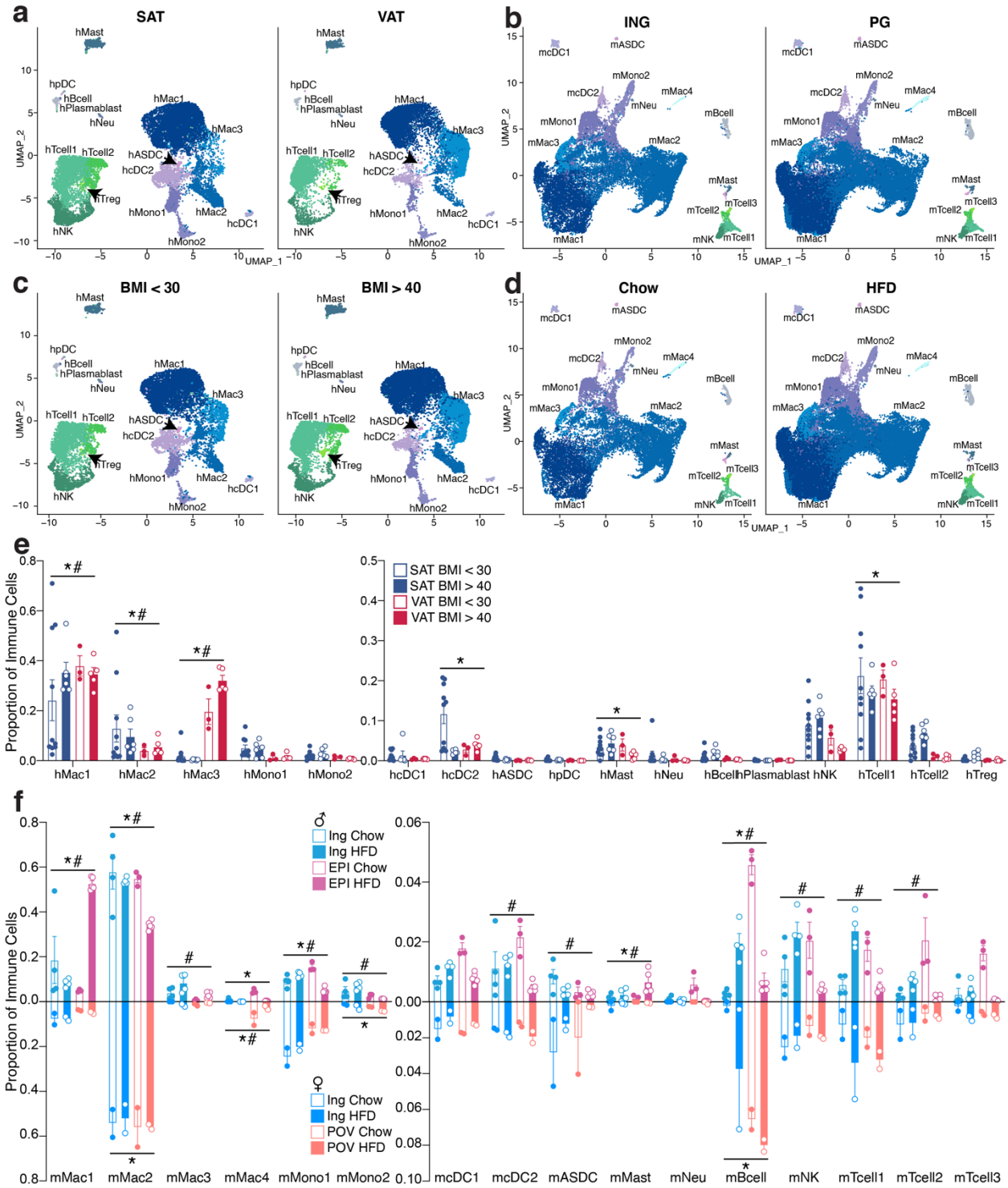
1111 **Extended Data Fig. 4. Highly similar vascular cells in human and mouse WAT. a,** UMAP  
 1112 projection of 22,734 human vascular cells. **b,** Marker genes for 11 distinct clusters of human  
 1113 WAT vascular cells. **c,** UMAP projection of 7,632 mouse vascular cells. **d,** Marker genes for 9  
 1114 distinct clusters of mouse WAT vascular cells. **e,** Riverplot showing the correlation between  
 1115 annotated mouse and human vascular clusters based on multimodal reference mapping for each

1116 mouse cell. **f-g**, Bar graphs showing the proportion of cells in each cluster per sample split by  
1117 depot and BMI for human (**f**) and depot, diet, and sex for mouse (**g**). For bar graphs, error bars  
1118 represent SEM, \* indicates credible depot effect and # indicates credible BMI/diet effect,  
1119 calculated using hEndoA2 (human) and mEndoA2 (mouse) as reference.



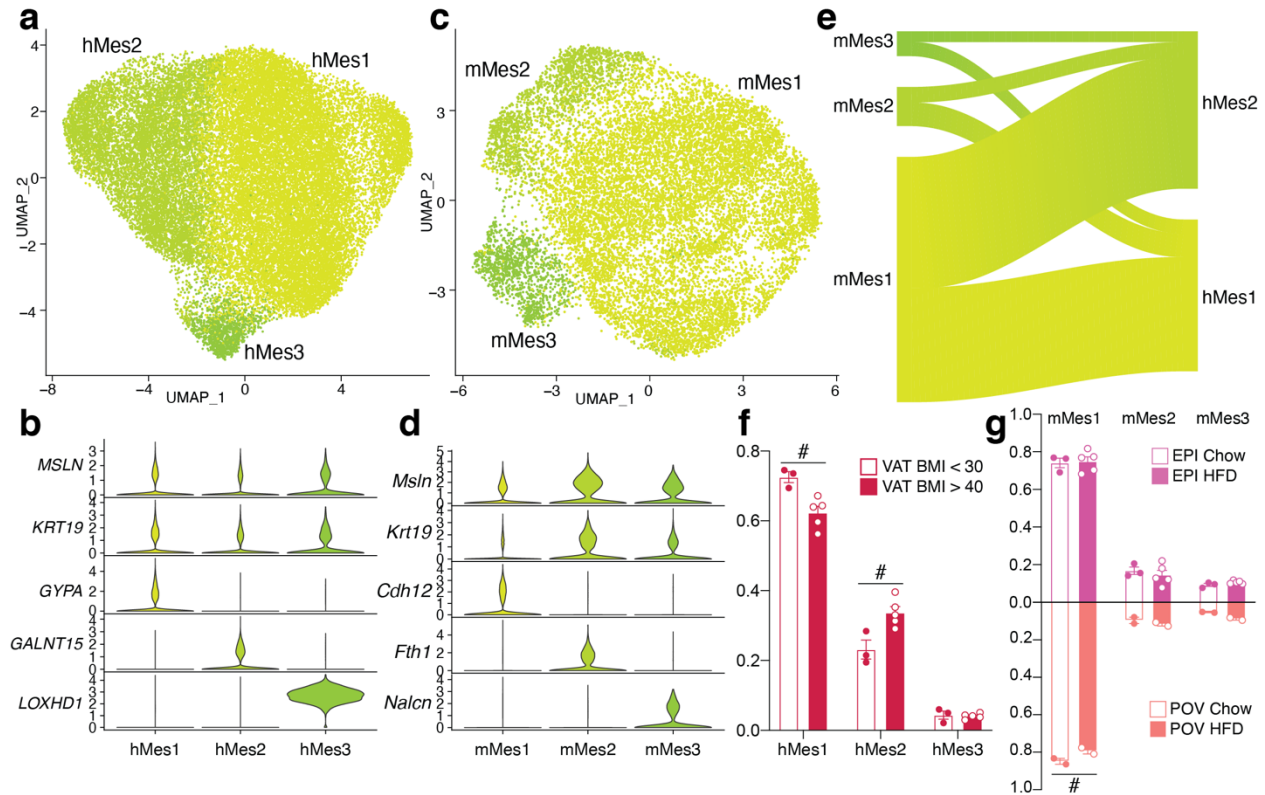


1120 **Extended Data Fig. 5. Comparison of immune cells in human and mouse WAT. a**, UMAP  
1121 projection of 34,268 immune cells from human WAT. **b**, Marker genes for human immune cell  
1122 clusters. **c**, UMAP projection of 70,547 immune cells from mouse WAT. **d**, Marker genes for  
1123 mouse immune cell clusters. **e-f**, Riverplots showing the correlation between annotated mouse  
1124 cluster and mapped human cluster for mouse (**e**) dendritic cells, mast cells, neutrophils, B cells,  
1125 NK cells, and T cells and (**f**) monocytes and macrophages.

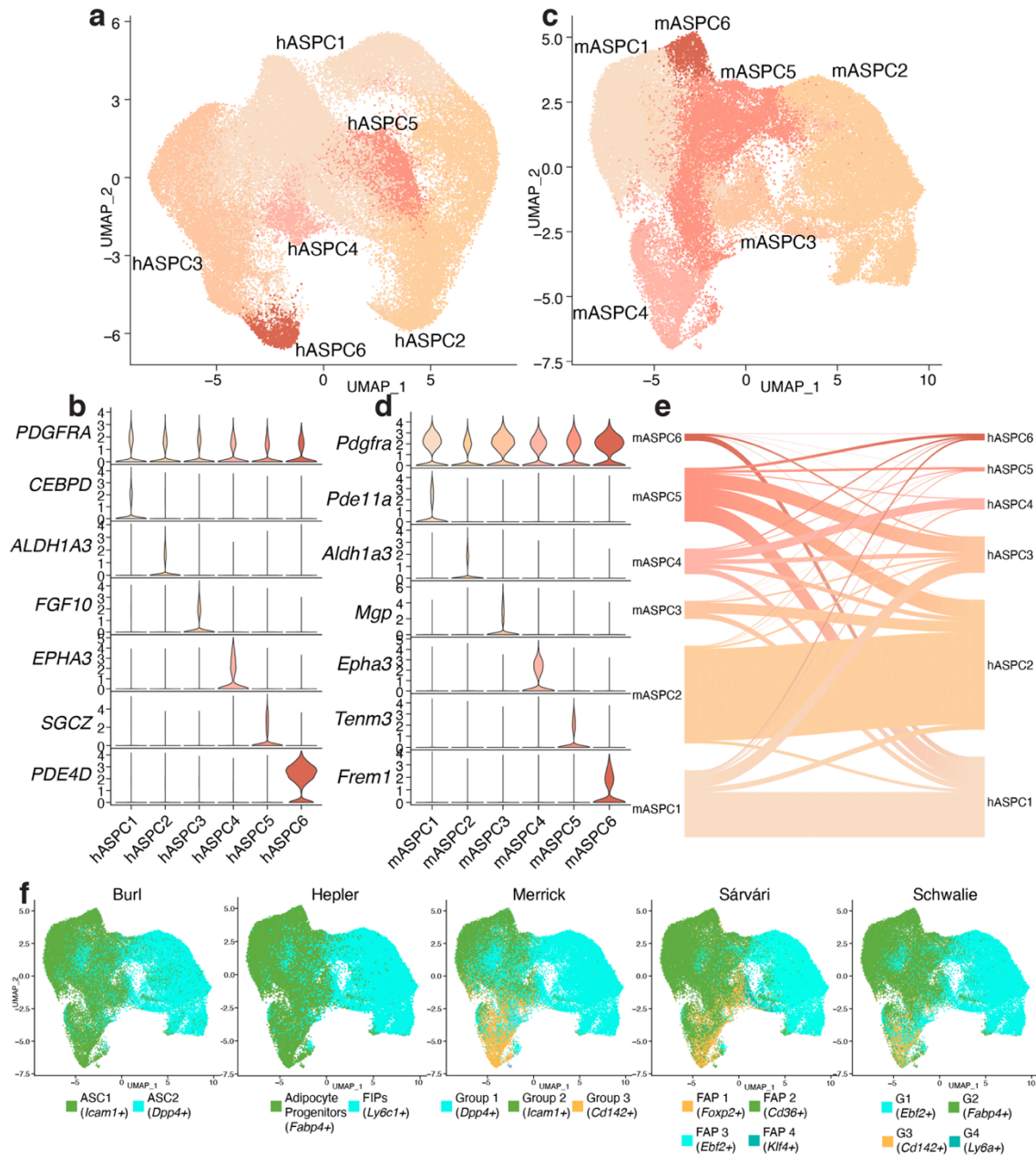


1126 **Extended Data Fig. 6. Human and mouse immune cells are differentially regulated by**  
 1127 **depot and BMI/diet. a-b,** UMAP projections of human (a) and mouse (b) WAT immune cells  
 1128 split by depot. c-d, UMAP projections of human (c) and mouse (d) WAT immune cells split by

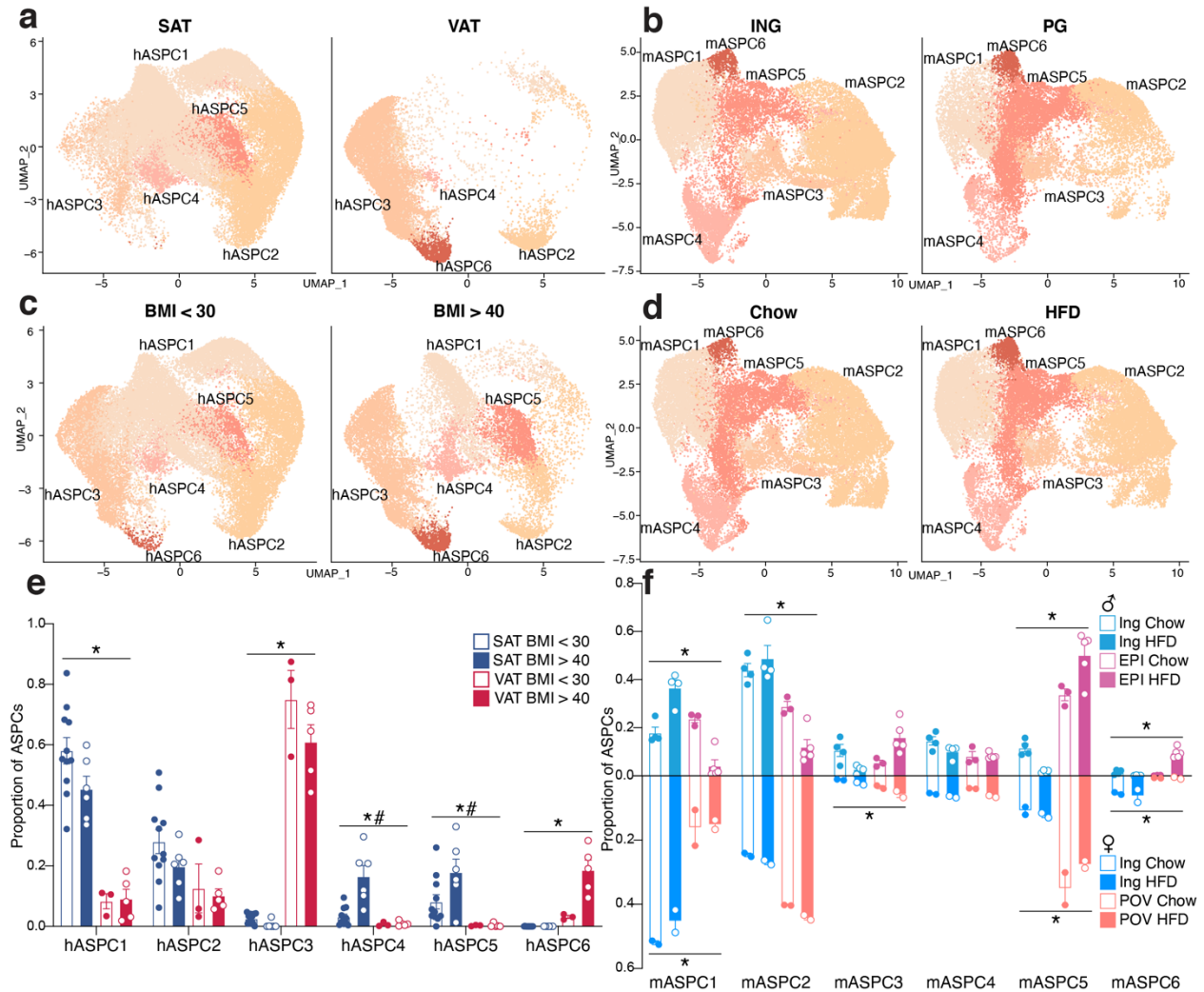
1129 BMI (**c**) and diet (**d**). **e-f**, Bar graphs showing the proportion of cells in each cluster per sample  
1130 split by depot and BMI for human (**e**) and depot, diet, and sex for mouse (**f**). For bar graphs,  
1131 error bars represent SEM, \* indicates credible depot effect and # indicates credible BMI/diet  
1132 effect, calculated using hMono2 (human) and mcDC1 (mouse) as reference.



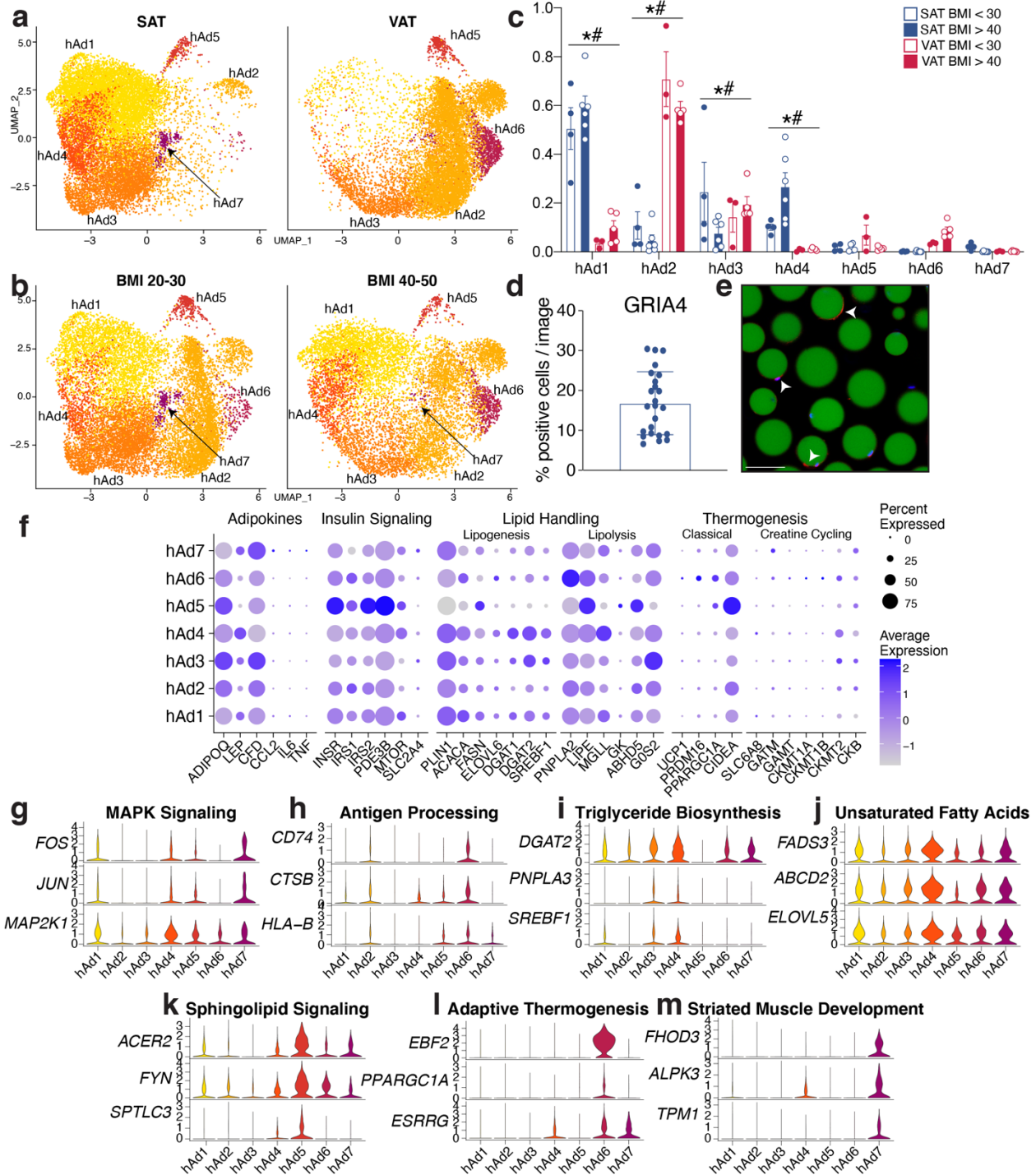
1133 **Extended Data Fig. 7. Subpopulations of human and mouse mesothelial cells. a**, UMAP  
 1134 projection of 30,482 human mesothelial cells. **b**, Marker genes for distinct human mesothelial  
 1135 populations. **c**, UMAP projection of 14,947 mouse mesothelial cells. **d** Marker genes for distinct  
 1136 mouse mesothelial populations. **e**, Riverplots showing relationship of mouse and human  
 1137 mesothelial clusters. **f-g**, Proportion of cells in each cluster per sample, split by BMI for human  
 1138 (**f**) and diet and sex for mouse (**g**). Error bars represent SEM, # indicates credible BMI/diet  
 1139 effect, calculated using hMes3 (human) and mMes1 (mouse) as reference.



1140 **Extended Data Fig. 8. Human and mouse ASPCs share commonalities with previously**  
 1141 **reported subtypes. a**, UMAP projection of 52,482 human ASPCs. **b**, Marker genes for distinct  
 1142 ASPC subpopulations. **c**, UMAP projection of 51,227 mouse ASPCs. **d**, Marker genes for  
 1143 distinct ASPC subpopulations. **e**, Riverplot depicting the relationship between mouse and human  
 1144 ASPC clusters. **f**, Reference mapping of ASPC cell types reported by other groups onto the  
 1145 mouse ASPCs from this paper.



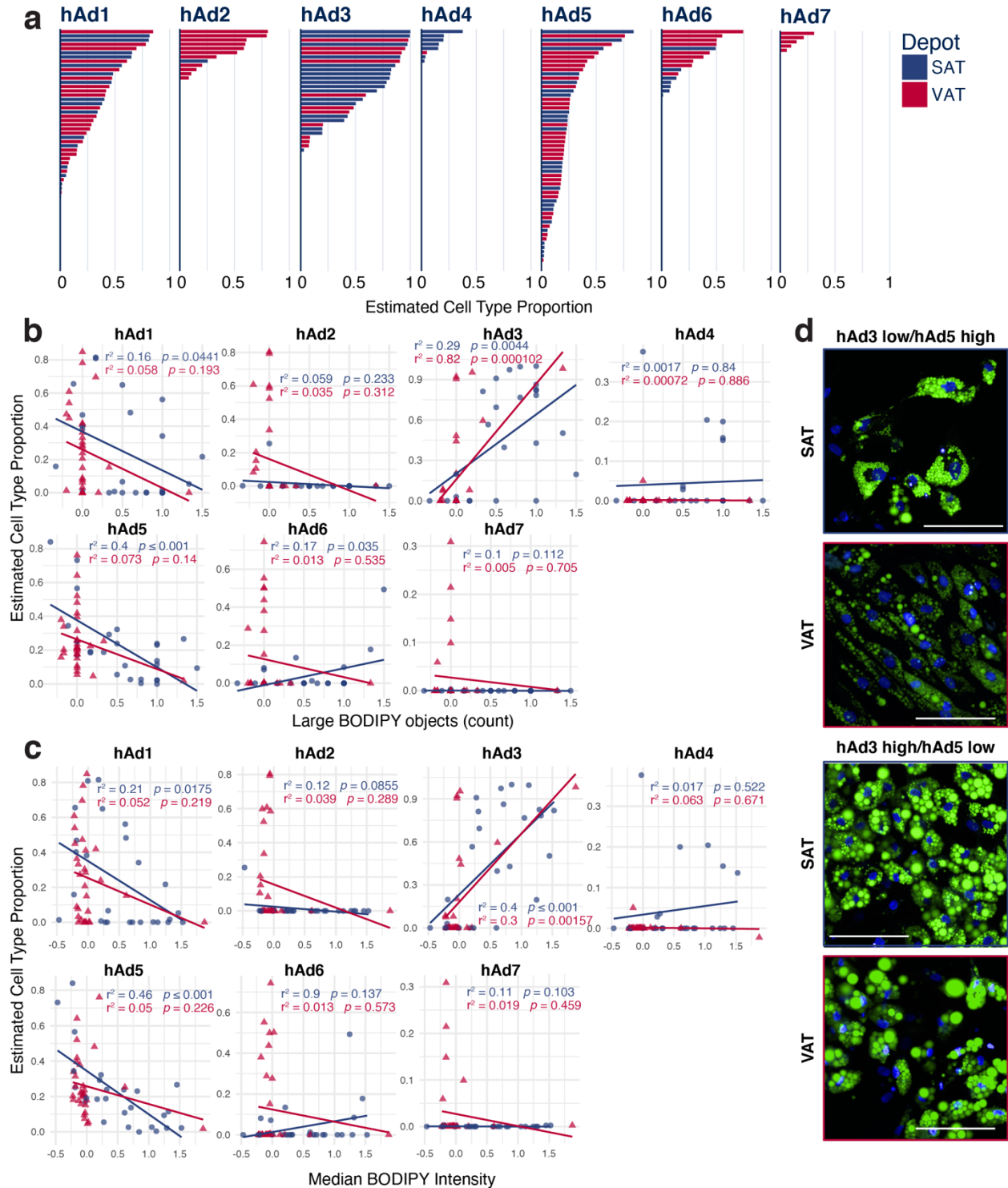
1146 **Extended Data Fig. 9. Human ASPCs exhibit strong depot dependency while mouse ASPCs**  
 1147 **are dependent on both depot and diet. a-b, UMAP projections of human (a) and mouse (b)**  
 1148 **ASPCs split by depot. c-d, UMAP projections of human (c) and mouse (d) ASPCs split by**  
 1149 **BMI/diet. e-f, Proportion of ASPC cells in each cluster per sample split by depot and BMI for**  
 1150 **human (e) and depot, diet, and sex for mouse (f). For bar graphs, error bars represent SEM, \***  
 1151 **indicates credible depot effect and # indicates credible BMI/diet effect, calculated using hASPC2**  
 1152 **(human) and mASPC4 (mouse) as reference.**



1153 **Extended Data Fig. 10. Human adipocyte subtypes are highly dependent on depot and may**  
 1154 **be responsible for distinct functions. a-b**, UMAP projections of human white adipocytes split  
 1155 by depot (**a**) and BMI (**b**). **c**, Proportion of cells in each human cluster by sample split by depot

1156 and BMI. **d**, Quantification of immunofluorescence analysis of GRIA4+ cells in mature human  
1157 adipocytes from two individuals. Each dot represents an image. **e**, Representative images of  
1158 GRIA4+ cells. **f**, Expression of genes associated with adipokine secretion, insulin signaling, lipid  
1159 handling, and thermogenesis across human adipocyte subclusters. **g-m**, Expression of genes  
1160 associated with GO or KEGG pathways indicative of individual human adipocyte subclusters.  
1161 For bar graph, error bars represent SEM, \* indicates credible depot effect and # indicates  
1162 credible BMI effect, calculated using hAd5 as reference.



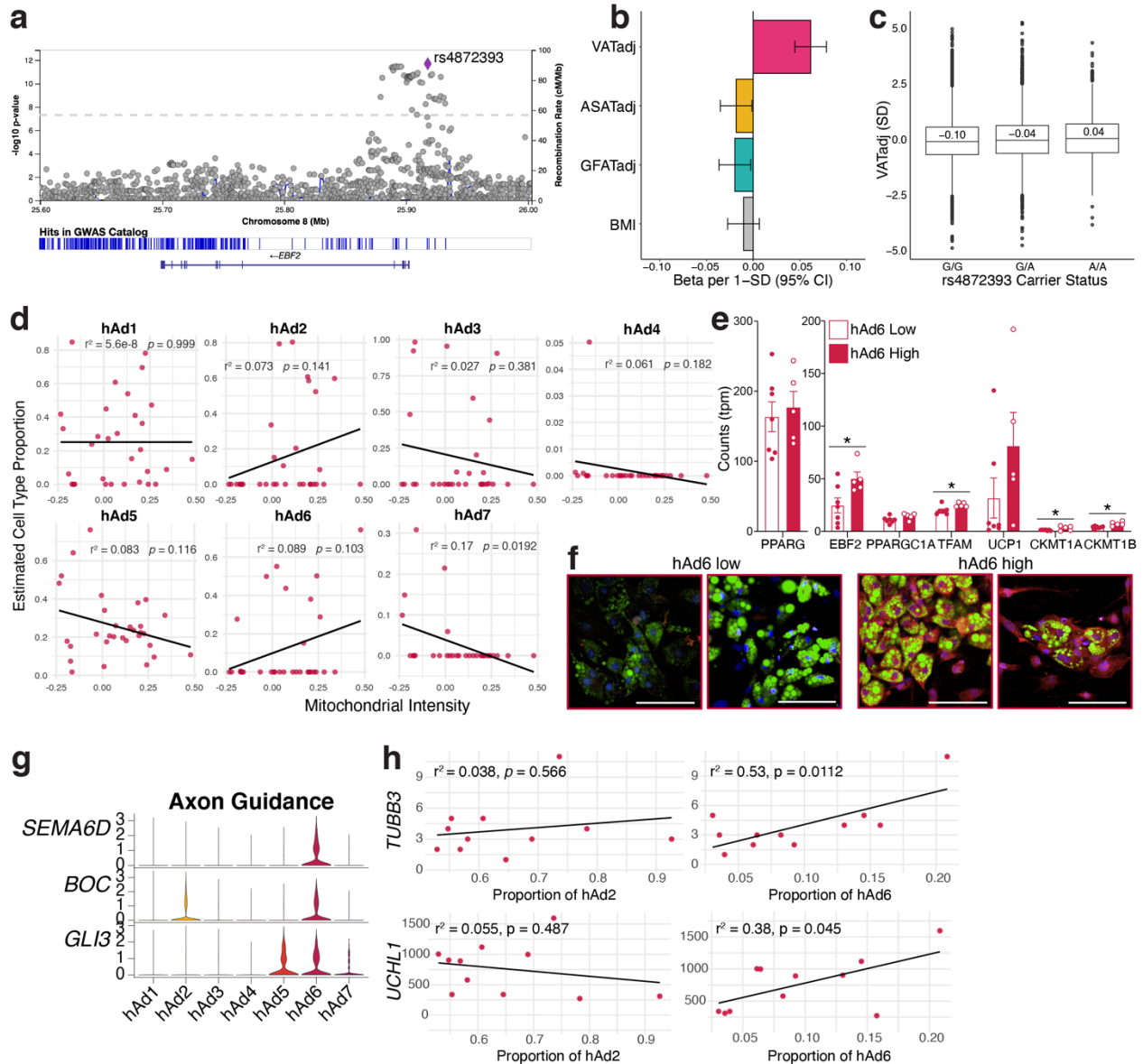


1163 **Extended Data Fig. 11. Human adipocytes differentiated ex vivo recapitulate many of the**

1164 **adipocyte subclusters found in vivo. a**, Plot of estimated cell type proportion in ex vivo

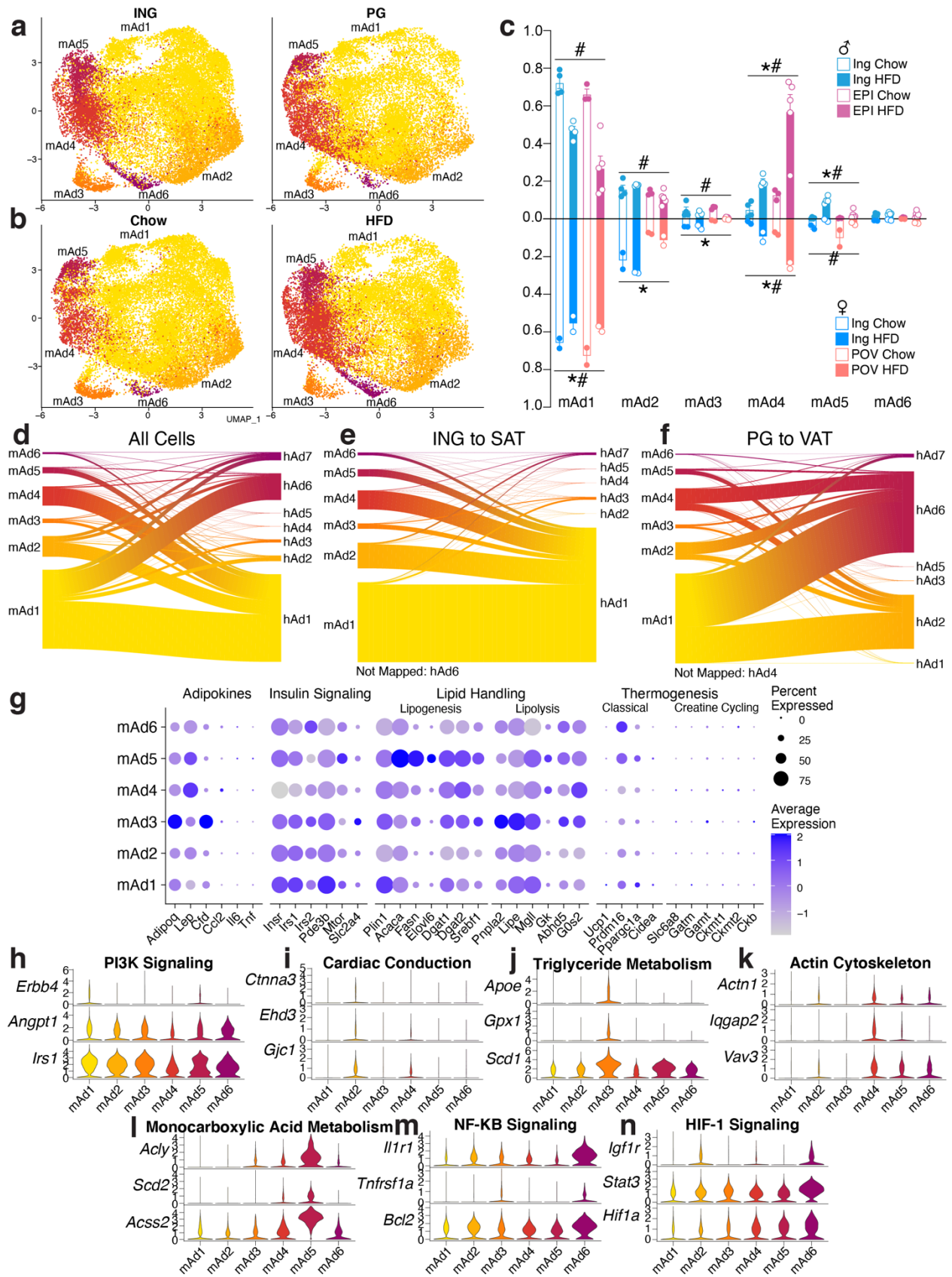
1165 adipocyte cultures differentiated from subcutaneous or visceral preadipocytes for 14 days,

1166 ordered by estimated proportion. **b-c**, Scatterplots showing the relationship between estimated  
1167 cell type proportion and the LipocyteProfiler-calculated features Large BODIPY objects (**b**) and  
1168 Median BODIPY Intensity (**c**). **d**, Representative images of hAd3 low/hAd5 or hAd3 high hAd5  
1169 low in vitro differentiated cultures. Green represents BODIPY staining, blue represents Hoechst  
1170 staining.

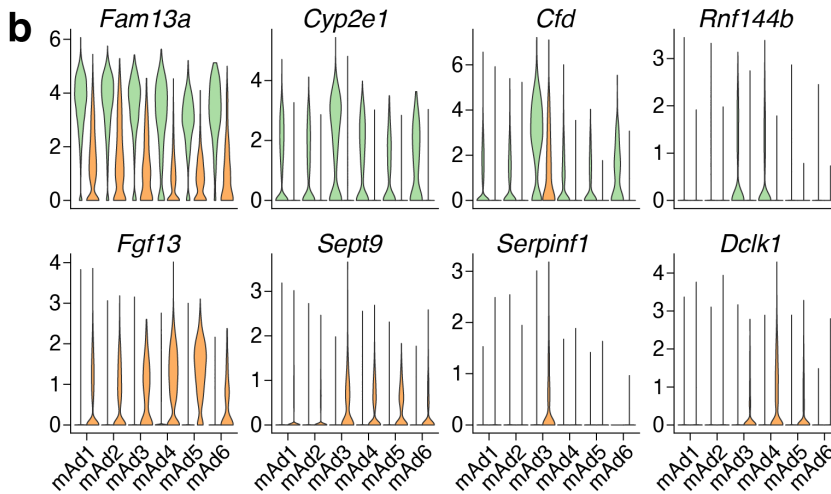
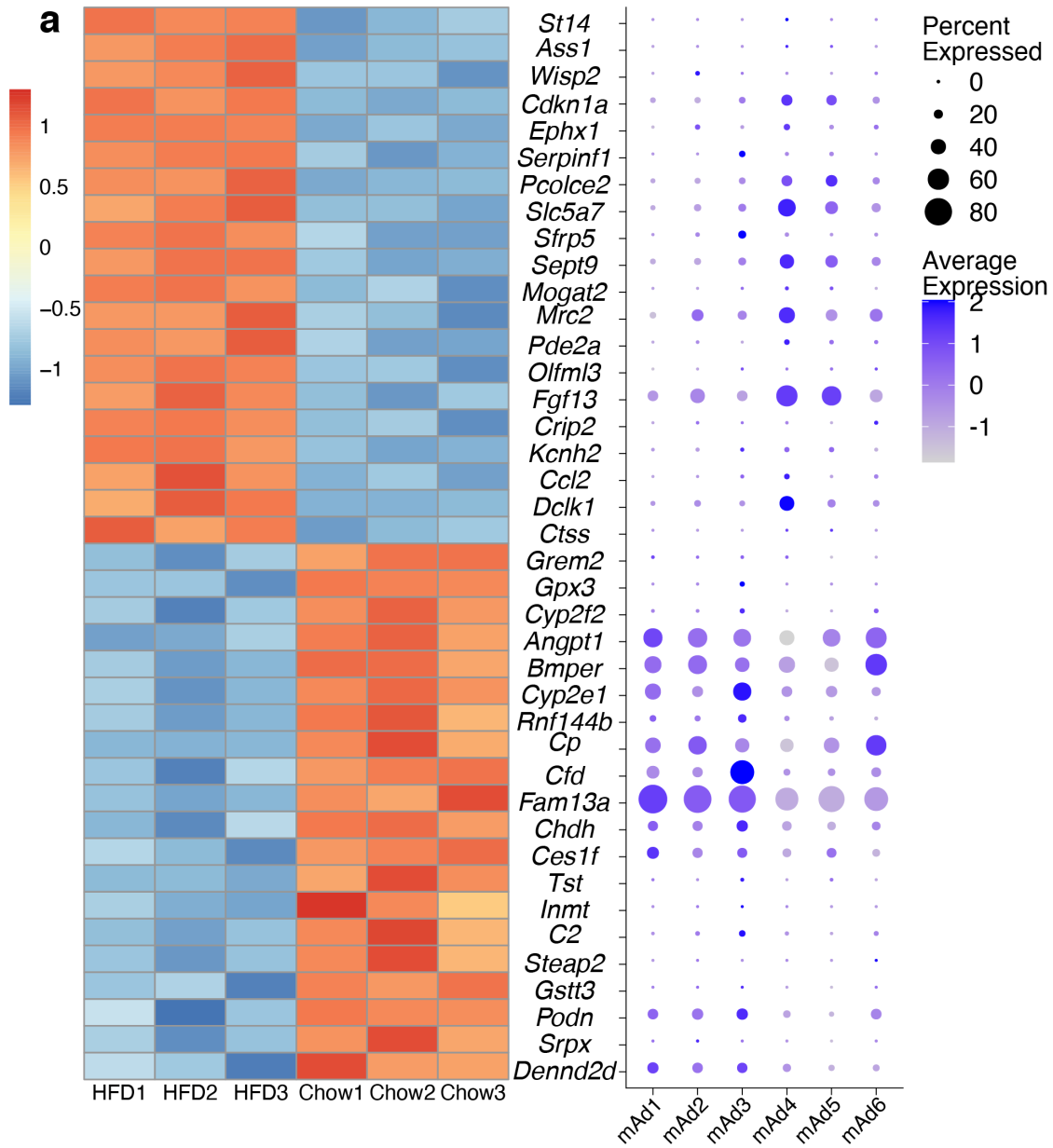


1171 **Extended Data Fig. 12. Visceral-specific adipocyte subpopulation hAd6 is associated with**  
 1172 **thermogenic traits.** **a**, Regional visualization of associations of common genetic variants near  
 1173 **EBF2** with VATadj. **b**, Association of rs4872393 with VATadj, ASATadj, GFATadj, and BMI  
 1174 per minor allele A; n = 37,641. **c**, VATadj raw data plotted according to rs4872393 carrier status;  
 1175 n = 36,185. **d**, Scatterplot showing the relationship between estimated cell type proportion and  
 1176 the LipocyteProfiler calculated feature Mitochondrial Intensity in visceral samples. **e**, Expression  
 1177 of mitochondrial and thermogenic genes in visceral in vitro differentiated adipocytes stratified by

1178 estimated hAd6 proportion and matched for amount of differentiation using *PPARG* levels. **f**,  
1179 Representative images of hAd6 low and high visceral in vitro differentiated cultures. Green  
1180 represents BODIPY staining, red represents MitoTracker staining, and blue represents Hoechst  
1181 staining. **g**, Violin plot of sNuc-seq data showing axon guidance genes in adipocyte subclusters.  
1182 **h**, Scatterplots showing the relationship between calculated proportion of visceral subpopulations  
1183 hAd2 and hAd6 and expression of pan-neuronal markers on the ambient RNA of individual  
1184 visceral sNuc-seq samples. For bar graph, error bars represent SEM, \*,  $p < .05$ , \*\*,  $p < .01$ .

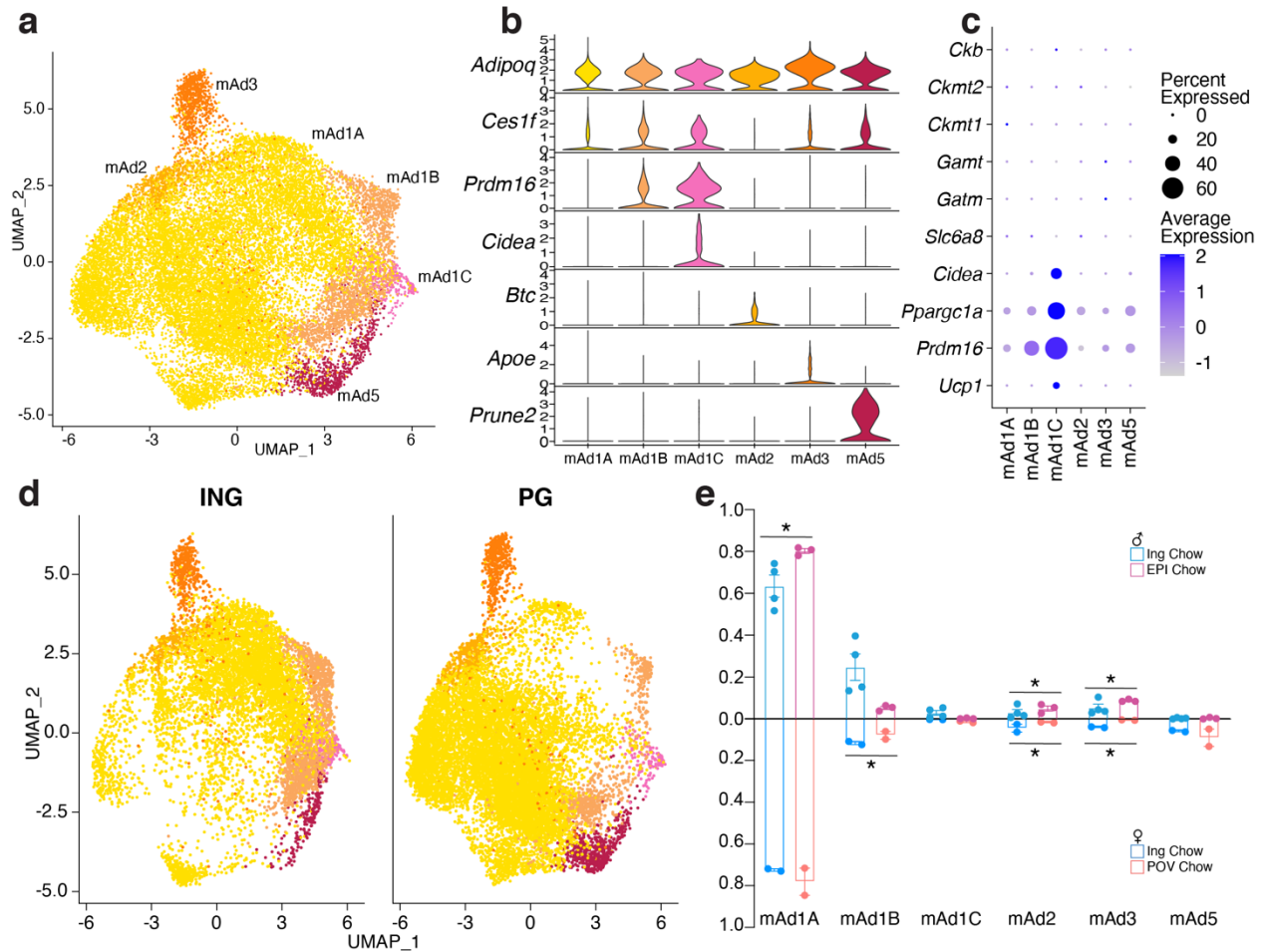


1185 **Extended Data Fig. 13. Mouse adipocytes appear to have distinct functionality but are not**  
1186 **analogous to human adipocyte subpopulations. a-b**, UMAP projections of mouse adipocytes  
1187 split by depot (**a**) and diet (**b**). **c**, Proportion of cells in each mouse cluster per sample split by  
1188 depot, diet, and sex. **d**, Expression of genes associated with known adipocyte functions in mouse  
1189 adipocyte subclusters. **e-k**, Expression of genes associated with GO or KEGG pathways  
1190 indicative of individual mouse adipocyte subclusters. **l-n**, Riverplots of mouse cells showing the  
1191 association between mouse and human adipocyte clusters from both subcutaneous and visceral  
1192 depots (**l**), subcutaneous (ING and SAT) adipocytes only (**m**) or visceral (PG and VAT)  
1193 adipocytes only (**n**). For depot comparisons, both mouse query objects and human reference  
1194 objects were subset to the respective depot before mapping. For bar graph, error bars represent  
1195 SEM, \* indicates credible depot effect and # indicates credible diet effect, calculated using  
1196 mAd6 as reference.

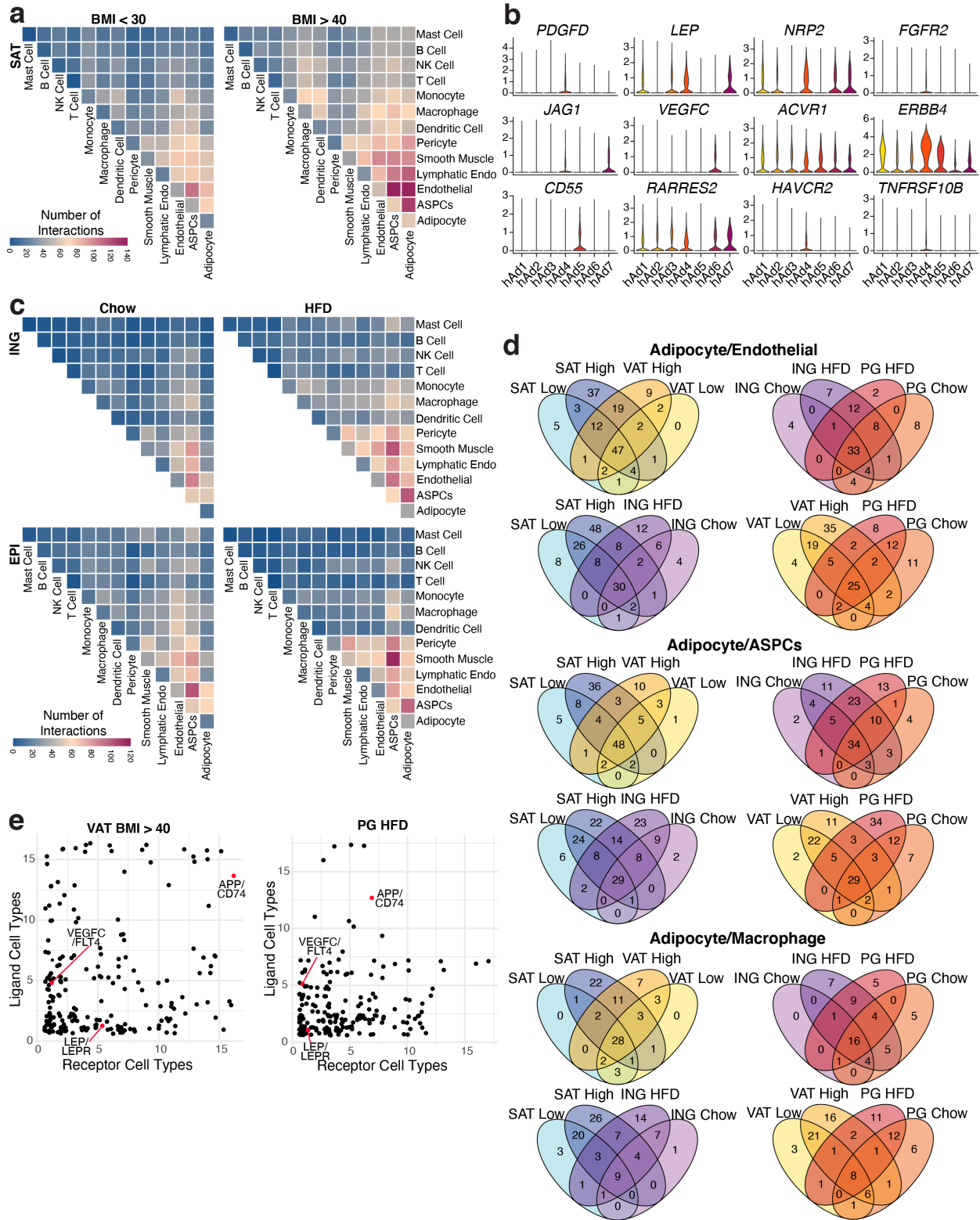


1197 **Extended Data Fig. 14. Adipocyte gene expression changes during high fat diet result from**  
1198 **both changes in abundance of adipocyte subtypes and from expression changes within**  
1199 **subclusters. a,** (left) Heatmap depicting expression of the top 20 most up- and down-regulated  
1200 genes in adipocytes after HFD feeding, as determined by bulk sequencing of TRAP-isolated  
1201 adipocyte RNA. On the right, the same genes are plotted onto the mouse adipocyte subclusters to  
1202 determine cluster specificity. **b,** Selected genes from **a** are plotted onto mouse adipocyte  
1203 subclusters and split by diet.





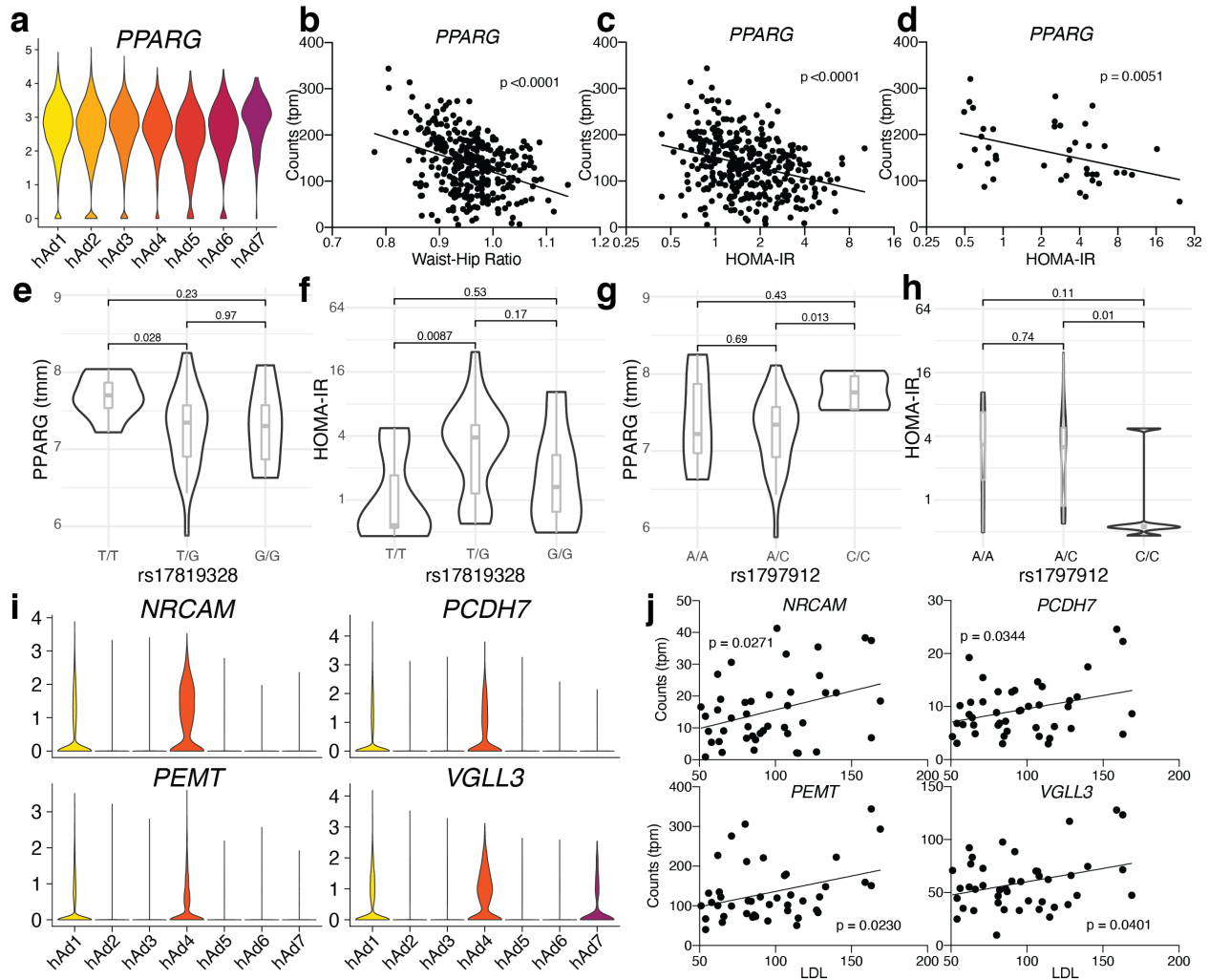
1204 **Extended Data Fig. 15. Mouse adipocytes from chow fed animals form a thermogenic**  
 1205 **subpopulation. a**, UMAP projection of 21,519 adipocytes from chow fed animals. **b**, Marker  
 1206 gene expression of adipocytes from chow fed mice. **c**, Thermogenic gene expression in mouse  
 1207 chow adipocyte subclusters. **d**, UMAP projection of adipocytes from chow fed animals split by  
 1208 depot. **e**, Proportion of cells in each sample by cluster split by depot and sex. Error bars represent  
 1209 SEM, \* indicates credible depot effect, calculated using mAd5 as reference.



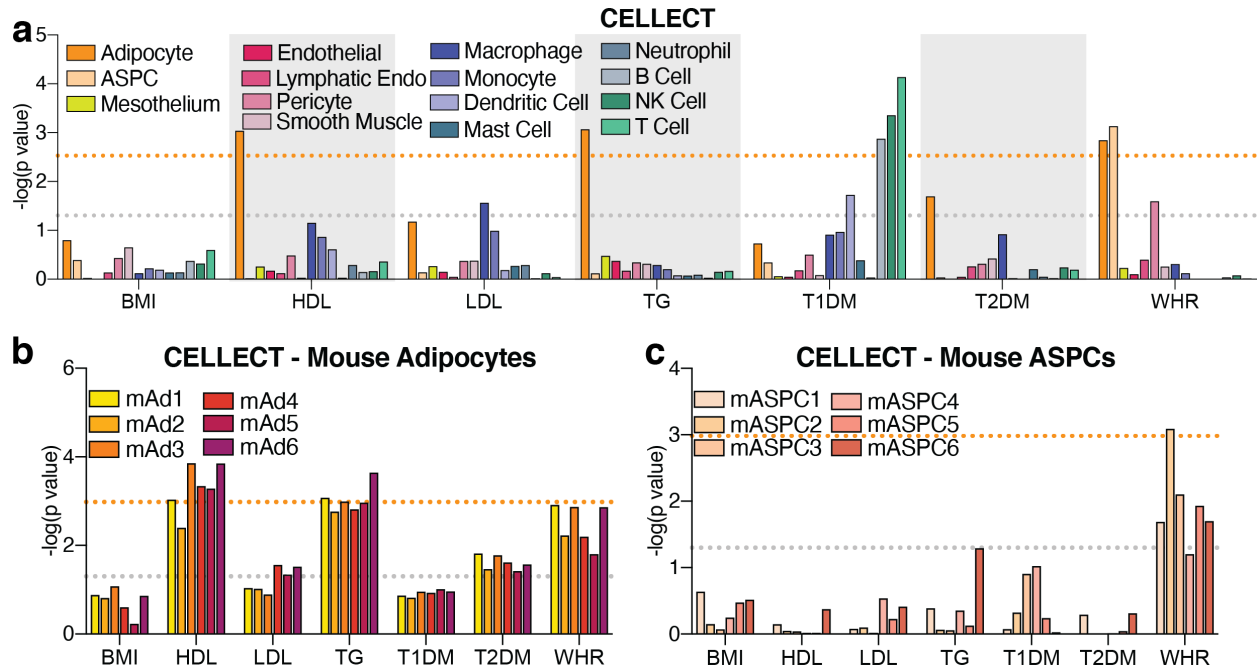
1210 **Extended Data Fig. 16. CellphoneDB identifies increasing numbers of cell-cell interactions**

1211 **within WAT during obesity. a, Heatmap showing number of significant interactions identified**

1212 between cell types in SAT of low (<30) and high (>40) BMI individuals as determined by  
1213 CellphoneDB. **b**, Expression levels of ligand and receptor genes from Figure 4b in human  
1214 adipocyte subclusters. **c**, Heatmaps showing number of significant interactions identified  
1215 between cell types in ING and PG WAT of chow and HFD fed mice. **d**, Venn diagrams showing  
1216 the overlap of significant interactions between adipocytes and endothelial cells, ASPCs, and  
1217 macrophages between depot, BMI/diet, and species. **e**, Jitter plots of the relationship between  
1218 number of WAT cell types expressing a ligand (y axis) vs. the number of cell types expressing  
1219 the receptor (x axis) for all significant interactions in high BMI human VAT (left) and mouse  
1220 HFD PG (right).



1221 **Extended Data Fig. 17. Association with GWAS data provides further insight into the**  
 1222 **contribution of human white adipocytes to human traits. a-c,** Expression of *PPARG* in  
 1223 human adipocyte subclusters (a), and in METSIM SAT bulk RNA-seq plotted against WHR (b)  
 1224 or HOMA-IR (c). **d,** Expression of *PPARG* in isolated subcutaneous adipocyte bulk RNA-seq  
 1225 plotted against HOMA-IR. **e-h,** SNPs in the *PPARG* gene identified by DEPICT as associated  
 1226 with BMI-adjusted WHR plotted against *PPARG* gene expression (e, g) and HOMA-IR (f, h) in  
 1227 isolated subcutaneous adipocyte bulk RNA-seq data and cohort. **i-j,** Expression of genes in  
 1228 human adipocyte subtypes from sNuc-seq data (i) and from isolated subcutaneous adipocyte bulk  
 1229 RNA-seq plotted against LDL levels (j).



1230 **Extended Data Fig. 18. CELLECT identifies mouse cell types associated with human**  
 1231 **GWAS studies. a**, *p* values of the association between mouse cell types and GWAS studies. **b-c**,  
 1232 *p* values of the association between mouse adipocyte (**b**) or ASC (**c**) subclusters with GWAS  
 1233 studies. For all graphs, the grey line represents  $p = 0.05$  and the orange line represents significant  
 1234 *p* value after Bonferroni adjustment ( $p = 0.003$  for all cell,  $p = 0.001$  for subclusters), calculated  
 1235 based on number of cell types queried.

1236 **Extended Data Table 1. Subject information for Drop-Seq, sNuc-seq, and bulk RNA-seq of**  
 1237 **isolated subcutaneous human adipocytes**

**Subjects for Drop-Seq**

Subject	BMI	Age	Sex	Race/Ethnicity	SAT	Surgery	Institution
Hs235	36.04	53	F	Caucasian	Pannus	Panniculectomy	BIDMC
Hs236	25.74	35	F	Caucasian	Thigh	Thighplasty	BIDMC
Hs237	22.59	53	F	Caucasian	Pannus	DIEP	BIDMC
Hs238	19.57	49	F	Caucasian	Pannus	Abdominoplasty	BIDMC
Hs239	24.8	71	F	Caucasian	Pannus	DIEP	BIDMC
Hs240	25.82	59	F	Caucasian	Pannus	Panniculectomy	BIDMC
Hs242	22.88	59	F	Caucasian	Pannus	DIEP	BIDMC
Hs248	32.28	68	F	Caucasian	Pannus	Panniculectomy	BIDMC
Hs249	26.46	54	F	Caucasian	Pannus	DIEP	BIDMC

DIEP: Deep inferior epigastric perforators

**Subjects for sNuc-seq**

Subject	BMI	Age	Sex	Race/ Ethnicity	SAT	VAT	Surgery	Institution
Hs001	49.3	29	F	Caucasian	Periumbilical	Omental	VSG	UPitt
Hs002	33.1	57	F	Caucasian	Periumbilical	NA	Hernia	UPitt
Hs004	25.4	51	F	Caucasian	Periumbilical	NA	CCY	UPitt
Hs009	45.7	41	F	Black	Periumbilical	Omental	VSG	UPitt
Hs010	43.1	35	F	Caucasian	Periumbilical	Omental	RYGB	UPitt
Hs011	42.8	58	F	Black	Periumbilical	NA	VSG	UPitt
Hs012	48.7	36	M	Caucasian	Periumbilical	Omental	VSG	UPitt
Hs013	43.2	24	M	Caucasian	Periumbilical	Omental	VSG	UPitt
Hs253	30.04	53	F	Caucasian	Periumbilical	Preperitoneal	TAH BSO	BIDMC
Hs254	23.96	41	F	Caucasian/ Hispanic	Periumbilical	Preperitoneal	TAH BSO	BIDMC
Hs255	24.27	73	F	Caucasian	Periumbilical	Preperitoneal	TAH BSO	BIDMC
Hs256	34.53	41	F	Black	Periumbilical	Omental	CCY	BIDMC
Hs266	22.15	68	M	Caucasian	Periumbilical	Omental	Colon polyp	BIDMC

VSG: Vertical sleeve gastrectomy

CCY: Cholecystectomy

RYGB: Roux en Y gastric bypass

TAH BSO: Total abdominal hysterectomy and bilateral salpingo-oophorectomy

**Bulk RNA-seq of floated adipocytes**

	Insulin Sensitive average(min-max)	Insulin Resistant average(min-max)	<i>p</i> Value
N	16	27	
AGE	47.3 (36-63)	50.6 (33-71)	0.289
BMI	27.2 (21-33)	30.1 (21-42)	0.042
HOMA-IR	0.70 (0.46-0.88)	5.8 (2.1-24.5)	0.00012
HDL	70.5 (42-154)	54.1 (26-100)	0.022
LDL	93.2 (54-133)	97.9 (51-169)	0.651

1238 **Extended Data Table 2. Numbers of cells in human and mouse single cell experiments**  
 1239 **broken down by cluster, depot, BMI/diet, and technology**

**Human Cell Numbers**

BMI	VAT			SAT					VAT total	SAT total	Total
	sNuc			sNuc			Drop				
	< 30	30-40	> 40	< 30	30-40	> 40	< 30	> 30			
Adipocyte	5211	1011	5253	7611	2847	3938	0	0	11475	14396	25871
ASPCs	5938	1404	7304	6848	2703	7329	15195	5761	14646	37836	52482
Mesothelium	7773	1927	20782	0	0	0	0	0	30482	0	30482
Endothelial	2351	1030	2345	4231	2783	2059	577	107	5726	9757	15483
Lymphatic Endo	677	240	1138	195	130	305	168	48	2055	846	2901
Pericyte	381	109	254	353	132	172	60	3	744	720	1464
Smooth Muscle	448	360	423	709	621	237	83	5	1231	1655	2886
Macrophage	1908	630	6328	3121	1795	2871	1256	403	8866	9446	18312
Monocyte	98	41	173	187	155	549	359	387	312	1637	1949
Dendritic Cell	125	30	340	169	119	188	756	714	495	1946	2441
Mast Cell	111	27	139	210	294	298	66	23	277	891	1168
Neutrophil	7	9	4	98	12	14	0	2	20	126	146
B Cell	28	12	39	57	49	188	30	26	79	350	429
NK Cell	229	92	242	375	279	669	297	446	563	2066	2629
T Cell	762	382	1661	667	510	1522	977	713	2805	4389	7194
Endometrium	45	150	114	0	0	0	2	1	309	3	312
Total	26092	7454	46539	24831	12429	20339	19826	8639	80085	86064	166149

**Mouse Cell Numbers**

	PG		Ing		PG Total	Ing Total	Total
	Chow	HFD	Chow	HFD			
Adipocyte	12874	5139	8645	13276	18013	21921	39934
ASPCs	9928	10194	16308	14797	20122	31105	51227
Mesothelium	10074	4873	0	0	14947	0	14947
Endothelial	1521	673	1141	2261	2194	3402	5596
Lymphatic Endo	678	101	224	173	779	397	1176
Pericyte	62	170	56	309	232	365	597
Smooth Muscle	56	52	30	125	108	155	263
Macrophage	3788	35673	9370	9017	39461	18387	57848
Monocyte	975	2801	1286	2545	3776	3831	7607
Dendritic Cell	268	688	237	379	956	616	1572
Mast Cell	4	267	13	27	271	40	311
Neutrophil	23	9	8	7	32	15	47
B Cell	301	594	28	279	895	307	1202
NK Cell	110	215	67	282	325	349	674
T Cell	266	472	69	479	738	548	1286
Male Epithelial	3463	36	19	329	3499	348	3847
Female Epithelial	76	45	6331	3135	121	9466	9587
Total	44467	62002	43832	47420	106469	91252	197721

1240 **Extended Data Table 3. GWAS studies used for CELLECT analysis**

<b>Trait</b>	<b>Study/collection</b>
<b>BMI</b>	Pulit, S. L. et al. Meta-analysis of genome-wide association studies for body fat distribution in 694 649 individuals of European ancestry.
<b>HDL</b>	<a href="https://alkesgroup.broadinstitute.org/sumstats_formatted/">https://alkesgroup.broadinstitute.org/sumstats_formatted/</a>
<b>LDL</b>	<a href="https://alkesgroup.broadinstitute.org/sumstats_formatted/">https://alkesgroup.broadinstitute.org/sumstats_formatted/</a>
<b>T1D</b>	<a href="https://alkesgroup.broadinstitute.org/sumstats_formatted/">https://alkesgroup.broadinstitute.org/sumstats_formatted/</a>
<b>T2D (BMI adjusted)</b>	Mahajan, A. et al. Fine-mapping type 2 diabetes loci to single-variant resolution using high-density imputation and islet-specific epigenome maps.
<b>Triglycerides</b>	<a href="https://alkesgroup.broadinstitute.org/sumstats_formatted/">https://alkesgroup.broadinstitute.org/sumstats_formatted/</a>
<b>WHR (BMI adjusted)</b>	Loh, P.-R., Kichaev, G., Gazal, S., Schoech, A. P. & Price, A. L. Mixed-model association for biobank-scale datasets